Invited Articles

Sensitivity analysis of thermoacoustic instability with adjoint Helmholtz solvers

Matthew P. Juniper*
Engineering Department, University of Cambridge, Cambridge CB2 1PZ, United Kingdom

(Received 3 July 2018; published 21 November 2018)

Gas turbines and rocket engines sometimes suffer from violent oscillations caused by feedback between acoustic waves and flames in the combustion chamber. These are known as thermoacoustic oscillations and they often occur late in the design process. Their elimination usually requires expensive tests and redesign. Full scale tests and laboratory scale experiments show that these oscillations can usually be stabilized by making small changes to the system. The complication is that, while there is often just one unstable natural oscillation (eigenmode), there are many possible changes to the system. The challenge is to identify the optimal change systematically, cheaply, and accurately. This paper shows how to evaluate the sensitivities of a thermoacoustic eigenmode to all possible system changes with a single calculation by applying adjoint methods to a thermoacoustic Helmholtz solver. These sensitivities are calculated here with finite-difference and finite-element methods, in the weak form and the strong form, with the discrete adjoint and the continuous adjoint, and with a Newton method applied to a nonlinear eigenvalue problem and an iterative method applied to a linear eigenvalue problem. This is a detailed comparison of adjoint methods applied to thermoacoustic Helmholtz solvers. MATLAB codes are provided for all methods and all figures so that the techniques can be easily applied and tested. This paper explains why the finite difference of the strong form equations with replacement boundary conditions should be avoided and why all of the other methods work well. Of the other methods, the discrete adjoint of the weak form equations is the easiest method to implement; it can use any discretization and the boundary conditions are straightforward. The continuous adjoint is relatively easy to implement but requires careful attention to boundary conditions. The summation by parts finite difference of the strong form equations with a simultaneous approximation term for the boundary conditions is more challenging to implement, particularly at high order or on nonuniform grids. Physical interpretation of these results shows that the well-known Rayleigh criterion should be revised for a linear analysis. This criterion states that thermoacoustic oscillations will grow if heat release rate oscillations are sufficiently in phase with pressure oscillations. In fact, the criterion should contain the adjoint pressure rather than the pressure. In self-adjoint systems the two are equivalent. In non-self-adjoint systems, such as all but a special case of thermoacoustic systems, the two are different. Finally, the sensitivities of the growth rate of oscillations to placement of a hot or cold mesh are calculated, simply by multiplying the feedback sensitivities by a number. These sensitivities are compared successfully with experimental results. With the same technique, the influence of the viscous and thermal acoustic boundary layers is found to be negligible, while the influence of a Helmholtz resonator is found, as expected, to be considerable.

DOI: 10.1103/PhysRevFluids.3.110509

*http://www2.eng.cam.ac.uk/~mpj1001/MJ_biography.html; mpj1001@cam.ac.uk

I. INTRODUCTION

Rockets and jet engines have unrivaled power to weight ratios and are therefore ideal for aerospace applications. They are designed to operate in steady flow, in the sense that the time average flow is the same as the ensemble average flow. Sometimes, however, heat release rate oscillations lock into acoustic oscillations so violently that they cause excessive heat transfer, structural vibration, and even catastrophic failure [1]. These are known as thermoacoustic oscillations.

The thermoacoustic mechanism is similar to that of a piston engine but with an acoustic wave taking the place of the piston: When more heat release rate occurs during moments of high pressure and less heat release rate occurs during moments of low pressure, more work is done during the expansion phase of the acoustic cycle than is absorbed during the compression phase, causing oscillations to grow [2]. A complete analysis can be found in [3] (p. 226), where Chu writes that "if m' [mass injection] is in phase with p' [acoustic pressure], or F' [momentum injection] with u' [acoustic velocity] or Q' [fluctuating heat release rate] with T' [acoustic temperature] then energy will be continuously fed into the disturbance." This quote will be reexamined in Sec. VIII in light of the results in this paper.

A key component in this mechanism is the heat release rate's response to acoustic perturbations. As the ratio of air to fuel in gas turbines is increased in order to reduce nitrous oxide emissions, flames tend to become more responsive to acoustics [1]. As a consequence, thermoacoustic oscillations are increasingly problematic for gas turbines. Worse still, their behavior is exceedingly sensitive to small parameter or shape changes [4]. Oscillations therefore tend to reappear during the later stages of testing and are rarely predicted reliably by component tests and analysis [5–7].

The goal of rocket and gas turbine manufacturers is to design an engine that is linearly stable to thermoacoustic oscillations over the entire operating regime. Currently, this is achieved through (i) extensive testing, which is expensive, (ii) the avoidance of certain engine operating regimes, which reduces flexibility, and (iii) the retrofitting of passive dampers such as Helmholtz resonators, which add weight and modes of failure [6,8]. A systematic method to identify optimal stabilization strategies will speed up development, eliminate dangerous operating points, and either determine the optimal placement of passive dampers or remove the need for them entirely. Such a method can exploit three convenient facts: First, the requirement is for linear (rather than nonlinear) stability, meaning that the tools of linear analysis can be used; second, no more than a handful of thermoacoustic modes are ever unstable; third, usually many parameters of the system can be altered. The challenge is therefore to identify the most influential parameters for each mode and how they should be changed optimally to stabilize the system.

An ideal solution is to develop a faithful model of the thermoacoustic system's linear behavior and then to combine linear stability analysis [9] with adjoint methods [10]. The stability analysis identifies the handful of unstable eigenvalues. The adjoint methods then show, in a single calculation for each eigenvalue, how each eigenvalue is affected by every parameter in the system. While this sensitivity could be calculated with finite-difference calculations, this would require a single calculation for each parameter, which is too expensive. This gradient information enables efficient optimization through, for example, change of boundary conditions, change of flame shape, change of geometry, or optimal addition of feedback devices such as Helmholtz resonators.

Different families of linear thermoacoustic models exist in the literature: (i) Galerkin methods, in which the acoustic perturbation is projected onto a basis set, which is usually the pure acoustic modes of the system; (ii) traveling wave methods (known as network models), in which the acoustics are expressed as traveling waves; and (iii) Helmholtz methods, in which the Helmholtz equation with heat release is solved in the frequency domain using finite difference, finite volume, or finite element for spatial discretization. The Galerkin method is easy to write in adjoint form [11,12] but has convergence problems [13] and is not straightforward to apply in complex geometries. The traveling wave method is relatively easy to write in adjoint form [4,14] but is restricted to simple acoustics. Nevertheless, this method is extensively used in industry and is a promising route to early application of adjoint methods in thermoacoustics. For example, adjoint-based optimization

is applied in [15] to stabilize all the modes of a traveling wave model of a laboratory burner and in [16] to stabilize all the modes of a traveling wave model of an annular combustor, using the adjoint version of an industrial code, LOTAN [17,18].

This paper shows how to derive the adjoints for Helmholtz solvers with finite-difference and finite-element discretizations, in the weak form and the strong form, with different boundary implementations, with the discrete adjoint and the continuous adjoint, and with a Newton method applied to a nonlinear eigenvalue problem and an iterative method applied to a linear eigenvalue problem. The methods are described in one spatial dimension, but the principles scale readily to two and three dimensions.

Reference [19] contains an outline of the mathematical principles required for adjoint Helmholtz solvers with active iteration, but no numerical implementation or results. Since then there have been some applications of adjoint Helmholtz solvers in the literature: (i) to optimize acoustic damper placement [20], (ii) to speed up uncertainty quantification [21,22], and (iii) to investigate the effects of asymmetry in annular combustors [23]. Adjoints have been applied (in collaboration with the author) to the three-dimensional finite-volume-based thermoacoustic solver AVSP [24]. The Supplemental Material of [4] contains rudimentary direct and adjoint codes for a Galerkin method, a traveling wave method, a finite-difference Helmholtz solver, and a finite-element Helmholtz solver in order to demonstrate extreme sensitivity in thermoacoustics. The codes in [4] contain only Dirichlet boundary conditions, the discrete adjoint, and the Newton method. The current paper is a paper on thermoacoustic Helmholtz solvers containing (i) the summation by parts (SBP) finite-difference formulation with a simultaneous approximation term (SAT); (ii) Neumann and frequency-dependent Robin boundary conditions for all types of discretizations; (iii) details of the numerical methods; (iv) comparisons of all methods and explanations of the sources of numerical problems; (v) physical interpretations of the base state sensitivities, structural sensitivities, and receptivities; (vi) the conclusion that Rayleigh's criterion needs to be revised for non-self-adjoint systems; (vii) optimization using base state sensitivities; (viii) estimation of the influence of neglected phenomena using feedback sensitivities; and (ix) estimation of the influence of retrofitted components using feedback sensitivities. The presentation is pedagogical and contains numerical details that the experienced reader can skip. MATLAB codes are provided for the four discretizations, all boundary conditions, both types of adjoint, and both types of solution methods so that the reader can apply the techniques easily and experience firsthand some of the benefits and pitfalls of the different approaches.

II. MODEL

A. Governing equations for mass, momentum, and energy

In this section all equations are dimensional and are written in terms of pressure p, density ρ, temperature T, entropy ς, and velocity $\underline{\mathbf{u}}$. Each total quantity (denoted by a circumflex) is comprised of a mean (denoted by an overline) and an acoustic fluctuation (denoted by a tilde). Following [25], the behavior of a single-component gas is modeled by the equation of state, the definition of entropy for a perfect gas, and transport equations for mass, momentum, and entropy of the total quantities

$$\frac{\hat{p}}{\hat{\rho}} = r_g \hat{T}, \tag{1a}$$

$$\hat{\varsigma} - \varsigma_{\text{ref}} = c_p \ln \frac{\hat{T}}{T_{\text{ref}}} - r_g \ln \frac{\hat{p}}{p_{\text{ref}}}, \tag{1b}$$

$$\frac{D\hat{\rho}}{Dt} = -\hat{\rho} \nabla \cdot \hat{\underline{\mathbf{u}}}, \tag{1c}$$

$$\hat{\rho} \frac{D\hat{\underline{\mathbf{u}}}}{Dt} = -\nabla \hat{p}, \tag{1d}$$

$$\hat{\rho} \frac{D\hat{\varsigma}}{Dt} = \frac{r_g}{\hat{p}} \hat{q}_h, \tag{1e}$$

where c_p is the specific heat capacity at constant pressure, r_g is the specific gas constant, and $\hat{q}_h$ is the heat release rate per unit volume, which is nonzero over some region $h(\underline{\mathbf{x}})$. Small-amplitude acoustic fluctuations $(\tilde{\underline{\mathbf{u}}}, \tilde{p}, \tilde{\rho}, \tilde{\varsigma}, \tilde{T})$ are considered, superimposed onto a zero Mach number steady base flow $(\overline{p}, \overline{\rho}, \overline{\varsigma}, \overline{T})$. Following [3] (see Sec. III therein), the acoustic equations are further perturbed by adding fluctuating mass injection per unit volume per unit time $\epsilon\delta\tilde{\dot{m}}$, fluctuating body force per unit volume $\epsilon\delta\tilde{\mathbf{f}}$, and fluctuating heat release rate per unit volume per unit time $\epsilon\delta\tilde{q}$. These perturbations, when suitably combined, can describe any physical perturbation to the system (Sec. VI). The linearized equations for the acoustic fluctuations are

$$\frac{\tilde{p}}{\overline{p}} - \frac{\tilde{\rho}}{\overline{\rho}} - \frac{\tilde{T}}{\overline{T}} = 0, \tag{2a}$$

$$\tilde{\varsigma} = c_p \frac{\tilde{T}}{\overline{T}} - r_g \frac{\tilde{p}}{\overline{p}}, \tag{2b}$$

$$\frac{\partial \tilde{\rho}}{\partial t} + \tilde{\underline{\mathbf{u}}} \cdot \nabla \overline{\rho} + \overline{\rho} \nabla \cdot \tilde{\underline{\mathbf{u}}} = 0 + \epsilon\delta\tilde{\dot{m}}, \tag{2c}$$

$$\overline{\rho} \frac{\partial \tilde{\underline{\mathbf{u}}}}{\partial t} + \nabla \tilde{p} = 0 + \epsilon\delta\tilde{\mathbf{f}}, \tag{2d}$$

$$\frac{\partial \tilde{\varsigma}}{\partial t} + \tilde{\underline{\mathbf{u}}} \cdot \nabla \overline{\varsigma} = \frac{r_g}{\overline{p}} (\tilde{q}_h + \epsilon\delta\tilde{q}). \tag{2e}$$

If the gas is perfect then (1b) implies that $\nabla(\ln \overline{\rho} + \overline{\varsigma}/c_p) = (\nabla \ln \overline{p})/\gamma$, which is zero because $\overline{p}$ is uniform because the flow has zero Mach number. Combining this with (2a) and (2b) and substituting into (2c) divided by $\overline{\rho}$ plus (2e) divided by c_p gives the acoustic equations for mass and energy (3b) and momentum (2d) and (3a):

$$\frac{\partial \tilde{\underline{\mathbf{u}}}}{\partial t} + \frac{1}{\overline{\rho}} \nabla \tilde{p} = \frac{\epsilon\delta\tilde{\mathbf{f}}}{\overline{\rho}}, \tag{3a}$$

$$\frac{1}{\gamma} \frac{\partial}{\partial t} \left(\frac{\tilde{p}}{\overline{p}} \right) + \nabla \cdot \tilde{\underline{\mathbf{u}}} = \frac{\epsilon\delta\tilde{\dot{m}}}{\overline{\rho}} + \frac{\gamma - 1}{\gamma} \left(\frac{\tilde{q}_h}{\overline{p}} + \frac{\epsilon\delta\tilde{q}}{\overline{p}} \right). \tag{3b}$$

B. Heat release model

The heat release model is a distributed n-τ model adapted from [25]. The local heat release rate perturbation per unit volume $\tilde{q}_h(\underline{\mathbf{x}}, t)$ is proportional to the velocity $\tilde{\underline{\mathbf{u}}}$ in a reference direction $\hat{\underline{\mathbf{w}}}$ integrated over a measurement region $w(\underline{\mathbf{x}})$ some time $\tau(\underline{\mathbf{x}})$ earlier,

$$\tilde{q}_h(\underline{\mathbf{x}}, t) = \eta h(\underline{\mathbf{x}}) \int_\Omega w(\check{\underline{\mathbf{x}}}) \hat{\underline{\mathbf{w}}} \cdot \tilde{\underline{\mathbf{u}}}(\check{\underline{\mathbf{x}}}, t - \tau(\underline{\mathbf{x}})) d\check{\underline{\mathbf{x}}}, \tag{4}$$

where $h(\underline{\mathbf{x}})$ is a distribution of heat release in space such that $\int_\Omega h(\underline{\mathbf{x}}) d\underline{\mathbf{x}} = 1$ and $w(\underline{\mathbf{x}})$ is a distribution of measurement in space such that $\int_\Omega w(\underline{\mathbf{x}}) d\underline{\mathbf{x}} = 1$. The integral $\int_\Omega \tilde{q}_h(\underline{\mathbf{x}}) d\underline{\mathbf{x}}$ has units J s^{-1} and the velocity $\tilde{\underline{\mathbf{u}}}$ has units m s^{-1}, so the constant η has units J m^{-1}.

It is useful to express η in terms of the magnitude of the flame transfer function (FTF). If $w(\underline{\mathbf{x}})$ is set to a Dirac δ function at $\underline{\mathbf{x}}_w$ and $\tau(\underline{\mathbf{x}})$ is uniform in space and $\tilde{u}_w \equiv \hat{\underline{\mathbf{w}}} \cdot \tilde{\underline{\mathbf{u}}}$ then (4) becomes $\int_\Omega \tilde{q}_h(\underline{\mathbf{x}}, t) d\underline{\mathbf{x}} = \eta \tilde{u}_w(\underline{\mathbf{x}}_w, t - \tau)$. The FTF is nondimensional and has magnitude $|\mathrm{FTF}| = |(\int_\Omega \tilde{q}_h d\underline{\mathbf{x}})/\overline{\dot{Q}_h}|/|\tilde{u}_w(x_w)/\overline{u}|$, where $\overline{\dot{Q}_h} \equiv \int_\Omega \overline{q_h} d\underline{\mathbf{x}}$ is the mean heat release rate. Therefore,

$$|\eta| = \frac{\left| \int_\Omega \tilde{q}_h d\underline{\mathbf{x}} \right|}{|\tilde{u}_w(\underline{\mathbf{x}}_w)|} = |\mathrm{FTF}| \frac{\overline{\dot{Q}_h}}{\overline{u}} \tag{5}$$

with units J m^{-1}, as expected.

C. Nondimensionalization

For dimensional consistency between the base state sensitivity (Sec. V) and the feedback sensitivity (Sec. VI), three new variables are defined:

$$\check{m}_{\overline{\rho}} \equiv \frac{\check{m}}{\overline{\rho}}, \quad \tilde{\mathbf{f}}_{\overline{\rho}} \equiv \frac{\tilde{\mathbf{f}}}{\overline{\rho}}, \quad \check{q}_{\overline{p}} \equiv \frac{\check{q}}{\overline{p}}. \tag{6}$$

The velocity $\underline{\tilde{\mathbf{u}}}$ is eliminated by subtracting the divergence of (3a) from the time derivative of (3b). The specific volume is defined as $\overline{v} \equiv \overline{\rho}^{-1}$ and the thermal expansion factor as $\zeta \equiv (\gamma - 1)/\gamma$. The equations are nondimensionalized with the length of the combustion chamber L_c, the ambient pressure p_a, and the speed of sound in the ambient fluid $(\gamma p_a/\rho_a)^{1/2}$. The pressure is uniform, so $\overline{p} = p_a$ throughout. The reference density is p_a/c_a^2, which means that the nondimensional ambient density is γ. The nondimensional governing equation is

$$\frac{1}{\gamma}\frac{\partial^2 \tilde{p}^\star}{\partial t^{2\star}} - \nabla^\star \cdot (\overline{v}^\star \nabla^\star \tilde{p}^\star) = \frac{\partial}{\partial t^\star}\epsilon\delta\check{m}^\star_{\overline{\rho}} - \nabla^\star \cdot \epsilon\delta\tilde{\mathbf{f}}^\star_{\overline{\rho}} + \zeta\left(\frac{\partial}{\partial t^\star}\frac{\check{q}^\star_h}{\overline{p}^\star} + \frac{\partial}{\partial t^\star}\epsilon\delta\check{q}^\star_{\overline{p}}\right), \tag{7a}$$

where

$$\frac{\check{q}^\star_h}{\overline{p}^\star} = \frac{\eta^\star}{\overline{p}^\star} h^\star(\underline{\mathbf{x}}^\star) \int_\Omega w^\star(\underline{\check{\mathbf{x}}}^\star)\underline{\tilde{\mathbf{u}}}^\star(\underline{\check{\mathbf{x}}}^\star, t^\star - \tau^\star(\underline{\mathbf{x}}^\star))d\underline{\check{\mathbf{x}}}^\star. \tag{7b}$$

D. Reduction to one dimension

The analysis in the rest of this paper is performed in one spatial dimension on $x \in [0, 1]$. The results are compared with experiments on a Rijke tube with cross-sectional area S_c. All properties are assumed to be uniform over the cross section. In (4), the heat release rate distribution in three-dimensional (3D) space $h(\underline{\mathbf{x}})$ is replaced with $h(x)/S_c$, where $h(x)$ is the heat release rate distribution in 1D space, defined such that $\int_0^1 h(x)dx = 1$. The 1D nondimensional governing equation is

$$\frac{1}{\gamma}\frac{\partial^2 \tilde{p}^\star}{\partial t^{2\star}} - \frac{d}{dx^\star}\left(\overline{v}^\star \frac{d\tilde{p}^\star}{dx^\star}\right) = \frac{\partial}{\partial t^\star}\epsilon\delta\check{m}^\star_{\overline{\rho}} - \frac{d}{dx^\star}\epsilon\delta\tilde{\mathbf{f}}^\star_{\overline{\rho}} + \zeta\left(\frac{\partial}{\partial t^\star}\frac{\check{q}^\star_h}{\overline{p}^\star} + \frac{\partial}{\partial t^\star}\epsilon\delta\check{q}^\star_{\overline{p}}\right), \tag{8a}$$

where

$$\frac{\check{q}^\star_h}{\overline{p}^\star} = \frac{\eta^\star}{\overline{p}^\star S_c^\star} h^\star(x^\star) \int_0^1 w^\star(\check{x}^\star)\tilde{u}^\star(\check{x}^\star, t^\star - \tau^\star(x^\star))d\check{x}^\star. \tag{8b}$$

A nondimensional heat release factor is then defined as $n^\star \equiv \eta^\star/\overline{p}^\star S_c^\star$.

E. Modal decomposition to the frequency domain

The star that designated nondimensional variables is now dropped and a modal decomposition is performed by substituting $\tilde{p}(x, t) = p(x, s)e^{st}$ and $\tilde{u}(x, t) = u(x, s)e^{st}$. The momentum equation (3a), in the absence of forcing and in one dimension, becomes $s\overline{\rho}u = -dp/dx$, so the heat release term (8b) becomes

$$\frac{\dot{q}_h}{\overline{p}} = n(e^{-s\tau(x)})h(x) \int_0^1 -\frac{1}{s}\frac{w}{\overline{\rho}}(\check{x})\frac{dp}{dx}(\check{x})d\check{x}. \tag{9}$$

This is substituted into (8a), the remaining substitutions with e^{st} are performed, and $w_{\overline{\rho}} \equiv w/\overline{\rho}$ is defined, leading to

$$\frac{s^2}{\gamma}p - \frac{d}{dx}\left(\overline{v}\frac{dp}{dx}\right) = -\zeta n(e^{-s\tau(x)})h(x) \int_0^1 w_{\overline{\rho}}(\check{x})\frac{dp}{dx}(\check{x})d\check{x} + s\epsilon\delta\dot{m}_{\overline{\rho}} - \frac{d}{dx}\epsilon\delta\mathbf{f}_{\overline{\rho}} + \zeta s\epsilon\delta\dot{q}_{\overline{p}}. \tag{10}$$

F. Definition of an inner product

An inner product is defined between two functions $f(x)$ and $g(x)$ spanning $x \in [0, 1]$:

$$\langle f, g \rangle \equiv \int_0^1 f^*(x) g(x) dx. \tag{11}$$

G. Expression as an eigenvalue problem

The terms in ϵ are now removed and will be reintroduced in Sec. VI. Equation (10) can then be written as

$$G(s)p \equiv (A(s) - s^2 C)p = 0, \tag{12a}$$

where

$$A \equiv \frac{d}{dx}\left(\overline{v}\frac{d}{dx}\right) - \zeta n(e^{-s\tau})h\left\langle w_\rho^*, \frac{d}{dx}\right\rangle, \tag{12b}$$

$$C \equiv 1/\gamma. \tag{12c}$$

Equation (12) is satisfied for eigenvalues s with corresponding right eigenvectors p.

III. SOLVING THE DIRECT PROBLEM

In this paper, and in the corresponding MATLAB programs, the governing equations (12) are solved numerically with four different discretizations: (i) a finite-difference method applied to the strong form of (12) with replacement boundary conditions, labeled `FDS`, (ii) a finite-element method applied to the weak form of (12), labeled `FEW`; (iii) a finite-difference method applied to the weak form of (12), labeled `FDW`; and (iv) a summation by parts finite-difference method applied to the strong form of (12) with a simultaneous approximation term for the boundary conditions, labeled `SBP`. A finite-volume discretization has been applied to this problem in [22]. This section contains numerical details, even though they are straightforward, because they have implications for the adjoint problem.

A. Finite-difference method applied to the strong form (FDS)

A finite-difference spectral method adapted from [26] is applied to the strong form of the governing equations (12). The function $p(x)$ is represented by a polynomial of order N. In addition, $N + 1$ Gauss-Lobatto-spaced collocation points are defined at $x = x_i$, in the domain $x \in [0, 1]$. Following the convention in [26], these are ordered backward from x_{N+1} at $x = 0$ to x_1 at $x = 1$. The function $p(x)$ is expressed as the sum of $N + 1$ Chebyshev polynomials. The coefficients of this sum are defined uniquely by the $N + 1$ values of $p(x_i)$. These values are held in the $(N + 1)$ column vector $\mathbf{p}$. When the polynomial representing $p(x)$ is differentiated, its order reduces by 1 and therefore the polynomial representing $p'(x)$ can be defined uniquely by the values of $p'(x)$ at N collocation points. A unique difference matrix $\mathbf{D}$ is defined such that $\mathbf{p}' = \mathbf{D}\mathbf{p}$. $\mathbf{D}$ has size $(N + 1) \times (N + 1)$ and gives $\mathbf{p}'$ at the $N + 1$ collocation points, but has rank N because only N values are required to define $p'(x)$ uniquely.

The integral $\int_0^1 p\, dx$ is given by $\mathbf{m}^T\mathbf{p}$, where $\mathbf{m}$ is a column vector containing the weighting associated with each collocation point. These are calculated with Clenshaw-Curtis quadrature (see [26], Chap. 12). A diagonal matrix $\mathbf{M}$ is defined, which contains the elements of $\mathbf{m}$ along the diagonal. For reasons described in Sec. IV B, it is convenient to premultiply the discretized forms of (12) by $\mathbf{M}$. This preconditioning does not affect the eigenvalues s or the right eigenvectors $\mathbf{p}$. With this preconditioning, the discretized form of (12) is

$$\mathbf{G}(s)\mathbf{p} \equiv (\mathbf{A}(s) - s^2\mathbf{C})\mathbf{p} = 0, \tag{13a}$$

where

$$\mathbf{A} \equiv \mathbf{MDVD} - \mathbf{M}\zeta n(\mathbf{e}^{-s\tau})\mathbf{h}\mathbf{w}_{\overline{\rho}}^{T}\mathbf{MD}, \tag{13b}$$

$$\mathbf{C} \equiv \mathbf{M}/\gamma, \tag{13c}$$

where $\mathbf{e}^{-s\tau}$ is an $(N+1)\times(N+1)$ matrix containing $e^{-s\tau(x_i)}$ along the diagonal, $\mathbf{h}$ is an $N+1$ column vector containing $h(x_i)$, $\mathbf{w}_{\overline{\rho}}$ is an $N+1$ column vector containing $w_{\overline{\rho}}(x_i)$, and $\mathbf{V}$ is an $(N+1)\times(N+1)$ matrix containing $\overline{v}(x_i)$ along the diagonal. In the MATLAB programs, the collocation points $\mathbf{x}$, differentiation matrix $\mathbf{D}$, mass matrix $\mathbf{M}$, density profile $\mathbf{V}$, and heat release properties $\mathbf{h}(x)$, $\mathbf{w}_{\overline{\rho}}(x)$, and $\tau(x)$ are created with `mat_FD.m`. Matrices $\mathbf{A}$ and $\mathbf{C}$ in (13) are assembled within `mat_AC_FDS_DA.m`.

Equation (12) is a second-order ordinary differential equation for p and therefore requires two boundary conditions. It is solved on the domain $x \in [0, 1]$ with boundary conditions on p at $x = 0$ (upstream) and $x = 1$ (downstream). These boundary conditions are either homogeneous Dirichlet, $p = 0$, homogeneous Neumann, $p' = 0$, or Robin: $p' = -k_u p$ at $x = 0$ and $p' = +k_d p$ at $x = 1$. (The difference in sign arises because the surface normal at $x = 0$ has the opposite sign from that at $x = 1$.) The constant $k = s(\overline{\rho}/\gamma)^{1/2}(R-1)/(R+1)$, where R is the acoustic reflection coefficient. Homogenous Dirichlet boundary conditions could be applied at $x = 1$ by removing the top row and left column of $\mathbf{A}$ and $\mathbf{C}$. This has the advantage that $\mathbf{A}$ and $\mathbf{C}$ regain full rank but the practical disadvantage when coding that the matrices change size. Instead, in this paper, the replacement method is used: Homogenous Dirichlet boundary conditions are applied at $x = 1$ by setting the top row and left column of $\mathbf{A}$ and $\mathbf{C}$ to zero and then setting the top left element of $\mathbf{A}$ to 1. The same procedure is applied at $x = 0$ by altering the bottom rows and right columns of $\mathbf{A}$ and $\mathbf{C}$. Homogenous Neumann boundary conditions are applied by (i) replacing the top or bottom rows of $\mathbf{A}$ by the top or bottom rows of $\mathbf{D}$ and (ii) entering zero into the top left or bottom right elements of $\mathbf{C}$. Robin boundary conditions ($p' = kp$) are applied by following steps (i) and (ii) above and then subtracting k_d from the top left element of $\mathbf{A}$ or $-k_u$ from the bottom right element of $\mathbf{A}$. These boundary conditions are implemented in `fun_bcs_strong.m`. For all of these boundary conditions, the top and bottom rows of $\mathbf{A}$ can be multiplied by arbitrary (nonzero) constants c_d and c_u without affecting the eigenvalue s or right eigenvector $\mathbf{p}$. This has implications for the left eigenvector and adjoint eigenfunctions (Sec. IV B and Fig. 3). The generalized matrix eigenvalue problem $\mathbf{A}(s)\mathbf{p} = s^2\mathbf{C}\mathbf{p}$ is solved numerically (Sec. III E). Here $\mathbf{C}$ is noninvertible due to the zeros added when the boundary conditions are applied. This creates two infinite eigenvalues, with corresponding eigenfunctions, which are discarded.

B. Finite-element method applied to the weak form (FEW)

Using the inner product (11), the governing equation (12) is multiplied by a test function z, which can be complex and rearranged via integration by parts into the weak form

$$\langle z, (A(s) - s^2C)p\rangle = \left[z^*\overline{v}\frac{dp}{dx}\right]_0^1 - \left\langle \frac{dz}{dx}, \overline{v}\frac{dp}{dx}\right\rangle - \left\langle z, \zeta n(e^{-s\tau})h\left\langle w_{\overline{\rho}}^*, \frac{dp}{dx}\right\rangle\right\rangle - \left\langle z, \frac{s^2}{\gamma}p\right\rangle = 0. \tag{14}$$

In order to discretize (14), restrictions are now placed on the differentiability of z and p. Here $N+1$ grid points are defined at $x = x_{1,i}$, equispaced from $x = 0$ to $x = 1$. The functions $z(x)$ and $p(x)$ are defined to be piecewise linear (P1), with values z_i and p_i at the $N+1$ grid points at $x_{1,i}$. These are held as column vectors $\mathbf{z}_1$, $\mathbf{p}_1$, and $\mathbf{x}_1$. The derivatives $z'(x)$ and $p'(x)$ are therefore piecewise constant (P0) functions, which are discontinuous at $x_{1,i}$. It is convenient to define N new grid points $x_{0,i}$ at the mean points between $x_{1,i}$ and to hold the values z_i' and p_i' of these P0 functions at the N grid points at $x_{0,i}$. These are held as column vectors $\mathbf{z}_0'$, $\mathbf{p}_0'$, and $\mathbf{x}_0$. A difference matrix $\mathbf{D}_{01}$ is defined such that $\mathbf{p}_0' = \mathbf{D}_{01}\mathbf{p}_1$. A mean matrix $\overline{\mathbf{M}}_{01}$ is defined such that $\mathbf{x}_0 = \overline{\mathbf{M}}_{01}\mathbf{x}_1$. Further, $\mathbf{D}_{01}$

and $\overline{\mathbf{M}}_{01}$ map P1 functions to P0 functions and so have N rows and $N+1$ columns. They therefore both have rank N, as did the difference matrix $\mathbf{D}$ in Sec. III A.

The inner product $\langle f, g\rangle$ between two P1 functions is evaluated exactly by $\mathbf{f}^H\mathbf{M}_{11}\mathbf{g}$, where $\mathbf{M}_{11}$ is an $(N+1)\times(N+1)$ tridiagonal matrix. The inner product $\langle f, g\rangle$ between two P0 functions is evaluated exactly by $\mathbf{f}^H\mathbf{M}_{00}\mathbf{g}$, where $\mathbf{M}_{00}$ is an $N\times N$ diagonal matrix. The inner product $\langle f, g\rangle$ between a P0 and a P1 function is evaluated exactly by $\mathbf{f}^H\mathbf{M}_{01}\mathbf{g}$, where $\mathbf{M}_{01}$ is an $N\times(N+1)$ matrix. In this formulation, $\mathbf{M}_{01}=\mathbf{M}_{00}\overline{\mathbf{M}}_{01}$. Equation (14) can then be written in matrix form as

$$\mathbf{z}_1^H\mathbf{G}_{11}(s)\mathbf{p}_1 \equiv \mathbf{z}_1^H(\mathbf{A}_{11}-s^2\mathbf{C}_{11})\mathbf{p}_1 = 0, \tag{15a}$$

where

$$\mathbf{A}_{11} \equiv -\mathbf{D}_{01}^H\mathbf{M}_{00}\mathbf{V}_{00}\mathbf{D}_{01} - \mathbf{M}_{11}\zeta n(\mathbf{e}^{-s\tau_1})\mathbf{h}_1\mathbf{w}_{\overline{\rho}0}^T\mathbf{M}_{00}\mathbf{D}_{01}, \tag{15b}$$

$$\mathbf{C}_{11} \equiv \mathbf{M}_{11}/\gamma, \tag{15c}$$

where $\mathbf{V}_{00}$ is an $N\times N$ matrix containing $\overline{v}(x_{0,i})$ along the diagonal, $\mathbf{e}^{-s\tau_1}$ is an $(N+1)\times(N+1)$ matrix containing $e^{-s\tau(x_{1,i})}$ along the diagonal, $\mathbf{h}_1$ is an $N+1$ column vector containing $h(x_{1,i})$, and $\mathbf{w}_{\overline{\rho}0}$ is an N column vector containing $w_{\overline{\rho}}(x_{0,i})$. In the MATLAB programs, the points, differentiation matrices, and mass matrices are created with `mat_FE.m`. Matrices $\mathbf{A}_{11}$ and $\mathbf{C}_{11}$ are assembled with `mat_AC_FEW_DA.m`.

The boundary conditions are applied via the boundary term in (14). For homogeneous Neumann boundary conditions $p'=0$, this term is zero and no further action is required. For Robin boundary conditions, this term is $z^*\overline{v}_d k_d p$ at $x=1$ and $-z^*\overline{v}_u(-k_u)p$ at $x=0$. These are applied by adding $\overline{v}_d k_d$ to the top left element of $\mathbf{A}_{11}$ and $\overline{v}_u k_u$ to the bottom right element of $\mathbf{A}_{11}$. Neumann and Robin boundary conditions are therefore defined without involving any arbitrary constants. Dirichlet boundary conditions are applied using the method described in Sec. III A, which does involve an arbitrary constant. These boundary conditions are implemented in `fun_bcs_weak.m`. Equation (15) must be satisfied for arbitrary $\mathbf{z}_1$ and so reduces to solving the generalized matrix eigenvalue problem $\mathbf{A}_{11}\mathbf{p}_1 = s^2\mathbf{C}_{11}\mathbf{p}_1$. The vector $\mathbf{z}_1$ contains $N+1$ elements, so there are $N+1$ equations with which to calculate the $N+1$ unknowns in the vector $\mathbf{p}_1$ and the problem is well posed if $\mathbf{A}_{11}$ has rank $N+1$. This is satisfied unless there are Neumann boundary conditions at both ends, in which case there is also a solution with a zero eigenvalue and a uniform eigenvector, which is discarded. For each Dirichlet boundary condition, there is an infinite eigenvalue and corresponding eigenvector, which is discarded.

C. Finite-difference method applied to the weak form (FDW)

The finite-difference scheme described in Sec. III A can also be applied to the weak form (14). Equation (14) can be written in matrix form as

$$\mathbf{z}^H\mathbf{G}\mathbf{p} \equiv \mathbf{z}^H(\mathbf{A}-s^2\mathbf{C})\mathbf{p} = 0, \tag{16a}$$

where

$$\mathbf{A} \equiv -\mathbf{D}^H\mathbf{M}\mathbf{V}\mathbf{D} - \mathbf{M}\zeta n(\mathbf{e}^{-s\tau})\mathbf{h}\mathbf{w}_{\overline{\rho}}^T\mathbf{M}\mathbf{D}, \tag{16b}$$

$$\mathbf{C} \equiv \mathbf{M}/\gamma, \tag{16c}$$

where the matrices are those from the finite-difference method (Sec. III A) and the boundary conditions are those from the finite-element method (Sec. III B). Matrices $\mathbf{A}$ and $\mathbf{C}$ are assembled with `mat_AC_FDW_DA.m`.

D. Summation by parts finite-difference method applied to the strong form (SBP)

In Sec. IV B it will be shown that the finite-difference method applied to the strong form equations with replacement boundary conditions (FDS), described in Sec. III A, produces

oscillations in the adjoint eigenvectors near the boundaries. This is because the FDS method is not dual consistent. One way to achieve a dual consistent method is to approximate the spatial derivatives with central-finite-difference operators that satisfy a SBP formula and then implement the boundary conditions with the SAT method [27–30].

Equation (12) requires a first derivative matrix $\mathbf{D}_1$ representing d/dx and a second derivative matrix with a nonhomogeneous coefficient $\mathbf{D}_2^{(\overline{v})}$ representing $d/dx[\overline{v}(x)d/dx]$. This second derivative matrix could be formed by applying the first derivative twice (see [31], pp. 506–507), but this leads to a wide stencil and, unless implemented carefully, to spurious oscillations. Alternatively, the second derivative matrix can be formed with a narrow stencil in which $\overline{v}(x_i)$ is embedded within the stencil (see [32], Appendix B). This narrow stencil avoids these spurious oscillations. Both $\mathbf{D}_1$ and $\mathbf{D}_2^{(\overline{v})}$ must satisfy the SBP formula: $\mathbf{D}_1$ must be expressible as $\mathbf{D}_1 = \mathbf{M}^{-1}\mathbf{Q}$, where $\mathbf{Q} + \mathbf{Q}^T = \text{diag}(+1, 0, \ldots, 0, -1)$ when $\mathbf{x}$ is ordered from $+1$ to 0; similarly, $\mathbf{D}_2^{(\overline{v})}$ must be expressible as $\mathbf{D}_2^{(\overline{v})} = \mathbf{M}^{-1}(-\mathbf{Y}^{(b)} + \tilde{\mathbf{V}}\mathbf{S})$, where $\mathbf{M}$ is the mass matrix $\text{diag}(0.5, 1, \ldots, 1, 0.5) \times dx$, $\mathbf{Y}^{(\overline{v})}$ is akin to a central-difference second-order derivative matrix, weighted by $\overline{v}(x_i)$, as described next, $\tilde{\mathbf{V}} = \text{diag}(-v_d, 0, \ldots, 0, v_u)$, and $\mathbf{S}$ approximates the first derivative operator at the boundaries.

In this paper, the second-order accurate central-difference scheme of Ref. [32] (see Appendix B therein) is applied, which satisfies a SBP formula. The matrix $\mathbf{Y}^{(\overline{v})}$, which is denoted by $M^{(b)}$ in [32], can be written as $\mathbf{D}_{01}^H\mathbf{M}_{00}\overline{\mathbf{V}}_{00}\mathbf{D}_{01}$, where $\mathbf{D}_{01}$ and $\mathbf{M}_{00}$ are identical to the matrices used in the finite-element method (FEW) in Sec. III B. The matrix $\overline{\mathbf{V}}_{00}$ is an $N \times N$ diagonal matrix containing $[\overline{v}(x_i) + \overline{v}(x_{i+1})]/2$ along the diagonal, i.e., the mean of the base density evaluated at adjacent grid points. To an excellent approximation, $\overline{\mathbf{V}}_{00}$ can be replaced by $\mathbf{V}_{00}$, which is an $N \times N$ diagonal matrix containing $\overline{v}[(x_i + x_{i+1})/2]$ along the diagonal, i.e., the base density evaluated at the mean of adjacent grid points. With this approximation, the SBP form of the strong form finite-difference equations (12) is

$$\mathbf{G}(s)\mathbf{p} \equiv (\mathbf{A} - s^2\mathbf{C})\mathbf{p} = 0, \tag{17a}$$

where

$$\mathbf{A} \equiv -\mathbf{D}_{01}^H\mathbf{M}_{00}\mathbf{V}_{00}\mathbf{D}_{01} + \tilde{\mathbf{V}}\mathbf{S} - \mathbf{M}\zeta n(\mathbf{e}^{-s\tau})\mathbf{h}\mathbf{w}_{\overline{\rho}}^T\mathbf{M}\mathbf{D}_1, \tag{17b}$$

$$\mathbf{C} \equiv \mathbf{M}/\gamma, \tag{17c}$$

where $\mathbf{e}^{-s\tau_1}$ is an $(N+1) \times (N+1)$ matrix containing $e^{-s\tau(x_{1,i})}$ along the diagonal, $\mathbf{h}$ is a $N+1$ column vector containing $h(x_{1,i})$, and $\mathbf{w}_{\overline{\rho}}$ is an $N+1$ column vector containing $w_{\overline{\rho}}(x_{1,i})$. In the MATLAB programs, the points, differentiation matrices, and mass matrices are created with `mat_SBP.m`. Matrices $\mathbf{A}$ and $\mathbf{C}$ are assembled with `mat_AC_SBP_DA.m`.

Robin and Neumann boundary conditions are applied by adding a SAT to the top and bottom rows of $\mathbf{A}$:

$$\mathbf{A} \leftarrow \mathbf{A} - \text{diag}(0, \ldots, 0, 1)(-k_u\overline{v}_u\mathbf{I} + \tilde{\mathbf{V}}\mathbf{S}) - \text{diag}(1, 0, \ldots, 0)(-k_d\overline{v}_d\mathbf{I} + \tilde{\mathbf{V}}\mathbf{S}). \tag{18}$$

This is adapted from [31] [see Eq. (A.3) therein] and [32] [see Eq. (3.7) therein]. Weak Dirichlet boundary conditions can be applied with Eq. (3.8) of [32] or equivalently by giving k_u and k_d large magnitudes.

E. Iteration procedures

The nonlinear matrix eigenvalue problems (13)–(17) are solved iteratively using two procedures, both of which are applied within `fun_Helm.m`. The first is a Newton method applied to the nonlinear eigenvalue problem $|\mathbf{G}(s)| = 0$, using Jacobi's formula for the derivative of a determinant of a matrix:

$$s_{j+1} = s_j - |\mathbf{G}|/(d|\mathbf{G}|/ds)_j = s_j - 1/[\text{tr}(\mathbf{G}^{-1}d\mathbf{G}/ds)]_j. \tag{19}$$

TABLE I. Dimensional quantities, reference quantities, and nondimensional quantities for the Rijke tube in [33] and a simplified model of a H_2/LOx rocket engine.

Rijke tube			Rocket engine		
		Dimensional quantities			
$\overline{\rho}$	($\mathrm{kg\,m^{-3}}$)	1.22	$\overline{\rho}$	($\mathrm{kg\,m^{-3}}$)	2.17
$\overline{p}$	(Pa)	$1.00 \times 10^{+5}$	$\overline{p}$	(Pa)	$1.00 \times 10^{+7}$
L_c	(m)	1.00	L_c	(m)	1.00
S_c	($\mathrm{m^2}$)	1.73×10^{-3}	S_c	($\mathrm{m^2}$)	5.03×10^{-1}
η	($\mathrm{J\,m^{-1}}$)	$2.80 \times 10^{+1}$	η	($\mathrm{J\,m^{-1}}$)	$2.00 \times 10^{+8}$
τ	(s)	1.50×10^{-3}	τ	(s)	1.00×10^{-4}
X_w	(m)	0.200	X_w	(m)	0.060
L_w	(m)	0.025	L_w	(m)	0.020
X_h	(m)	0.250	X_h	(m)	0.700
L_h	(m)	0.025	L_h	(m)	0.100
$\overline{\rho_u}$	($\mathrm{kg\,m^{-3}}$)	1.220	$\overline{\rho_u}$	($\mathrm{kg\,m^{-3}}$)	2.165
$\overline{\rho_d}$	($\mathrm{kg\,m^{-3}}$)	0.850	$\overline{\rho_d}$	($\mathrm{kg\,m^{-3}}$)	2.165
		Reference quantities			
L_{ref}	(m)	1.00	L_{ref}	(m)	1.00
p_{ref}	(Pa)	$1.00 \times 10^{+5}$	p_{ref}	(Pa)	$1.00 \times 10^{+7}$
u_{ref}	($\mathrm{m\,s^{-1}}$)	339	u_{ref}	($\mathrm{m\,s^{-1}}$)	2506
		Nondimensional quantities			
γ		1.40	γ		1.36
R_u		$-0.975 + 0.050i$	R_u		$+0.999 + 0.000i$
R_d		$-0.975 + 0.050i$	R_d		$+0.695 + 0.000i$
n		0.161	n		39.789
τ		0.508	τ		0.251
X_w		0.200	X_w		0.060
L_w		0.025	L_w		0.020
X_h		0.250	X_h		0.700
L_h		0.025	L_h		0.100
ρ_u		1.400	ρ_u		1.360
ρ_d		0.975	ρ_d		1.360

This is rendered more stable by performing a QR decomposition on $\mathbf{G}$. No relaxation is used. Once the eigenvalue s has been found to sufficient tolerance, the eigenvector is the null space of $\mathbf{G}(s)$.

The second is the active iterative method described in Sec. IV.B of [25]. From a starting point, labeled s_0, subsequent solutions, labeled s_j, are obtained by solving the generalized linear eigenvalue problem $\mathbf{A}(s_{j-1})\mathbf{p} = s_j^2\mathbf{C}\mathbf{p}$ in which the frequency-dependent terms in $\mathbf{A}$ have been evaluated at s_{j-1}. This process is repeated J times. No relaxation is used. The eigenvector is calculated alongside the eigenvalue using `fun_eig_nearest.m`. In both cases there are several possible solutions and the converged solution depends on the choice of s_0. In this paper chamber modes [9] are being modeled, so it is appropriate to start from one of the natural acoustic modes of the chamber. This mode is specified by the user in `fun_param_dim.m`.

F. Results

The methods in this paper are demonstrated on (i) a model of the electrically heated Rijke tube in [33] and (ii) a simplified model of a rocket engine. For the Rijke tube, n is small and the peaks of $w_{\overline{\rho}}(x)$ and $h(x)$ are close, which causes the system to be nearly self-adjoint. For the rocket engine, n is large and the peaks of $w_{\overline{\rho}}(x)$ and $h(x)$ are widely separated, which causes the system to be strongly non-self-adjoint. It is instructive to compare the two. The dimensional quantities, reference quantities, and nondimensional quantities are listed in Table I. The distributions of $\overline{\rho}(x)$, $h(x)$, and

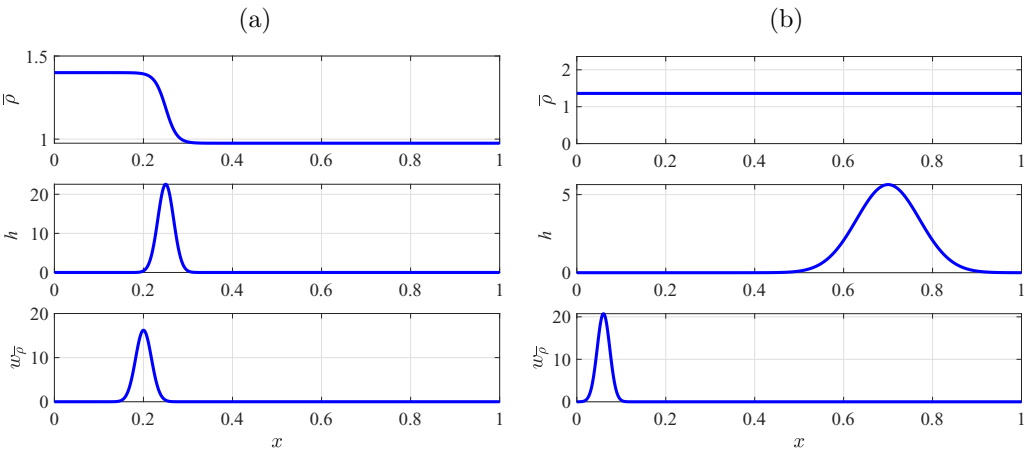

FIG. 1. Distributions of density $\overline{\rho}(x)$, heat release region $h(x)$, and measurement region $w_{\overline{\rho}}$ for (a) the Rijke tube in [33] and (b) a simplified model of a H_2/LOx rocket engine. The dimensional, reference, and nondimensional quantities are in Table I.

$w_{\overline{\rho}}(x)$ are shown in Fig. 1. The dimensional quantities are held in `fun_param_dim.m` and converted to reference quantities and nondimensional quantities in `fun_param_nondim.m`. The distributions are calculated in `fun_rh.m`, `fun_h.m`, and `fun_wr.m`.

The first eigenmode of each test case is shown in Fig. 2, calculated with the finite-difference method of the strong form (`FDS`), the finite-element method (`FEW`), the finite-difference method of the weak form (`FDW`), and the summation by parts finite-difference method of the strong form (`SBP`) using the nonlinear (`nonlin`) and linear (`linear`) iteration procedures. For presentation, the eigenfunctions have been normalized such that $\int p^2 dx = 1$. In each plot there are eight lines, which all lie on top of each other, showing that the eigenfunctions are identical to the eye. Studying the eigenvalues reveals that the two iteration procedures (`linear` and `nonlin`) converge to the same eigenvalues for each spatial discretization. The eigenvalues depend slightly on whether the Robin boundary conditions are enforced through replacement (`FDS`) or not (`FEW`, `FDW`, and `SBP`). Enforcing them through replacement is more accurate, with a boundary error of order 10^{-12} for `FDS`, as compared to a boundary error of order 10^{-3} for `FDS`, `FEW`, and `FDW`. This boundary error is displayed by toggling `show_boundary_error` in `fun_Helm.m`.

IV. SOLVING THE ADJOINT PROBLEM

A. Definition of the adjoint eigenfunction and the left eigenvector

Equation (12) is the direct continuous eigenvalue problem in the strong form. Using the inner product (11), this can be premultiplied by a function $p^\dagger(x)$:

$$\langle p^\dagger, G(s)p\rangle \equiv \langle p^\dagger, (A(s) - s^2 C)p\rangle = 0. \tag{20}$$

For a given eigenvalue s, the corresponding direct eigenfunction $p(x)$ satisfies (20) for arbitrary $p^\dagger(x)$ and the corresponding adjoint eigenfunction $p^\dagger(x)$ satisfies (20) for arbitrary $p(x)$. This is the definition of the adjoint eigenfunction $p^\dagger(x)$.

There is an equivalent definition for the discretized problem. The corresponding generalized matrix eigenvalue problem (13) is premultiplied by a column vector $\mathbf{z}^H$:

$$\mathbf{z}^H \mathbf{G}(s)\mathbf{p} \equiv \mathbf{z}^H(\mathbf{A}(s) - s^2\mathbf{C})\mathbf{p} = 0. \tag{21}$$

For a given eigenvalue s, the corresponding right eigenvector $\mathbf{p}$ satisfies (21) for arbitrary $\mathbf{z}$ and the corresponding left eigenvector $\mathbf{z}$ satisfies (21) for arbitrary $\mathbf{p}$. This is the definition of the left

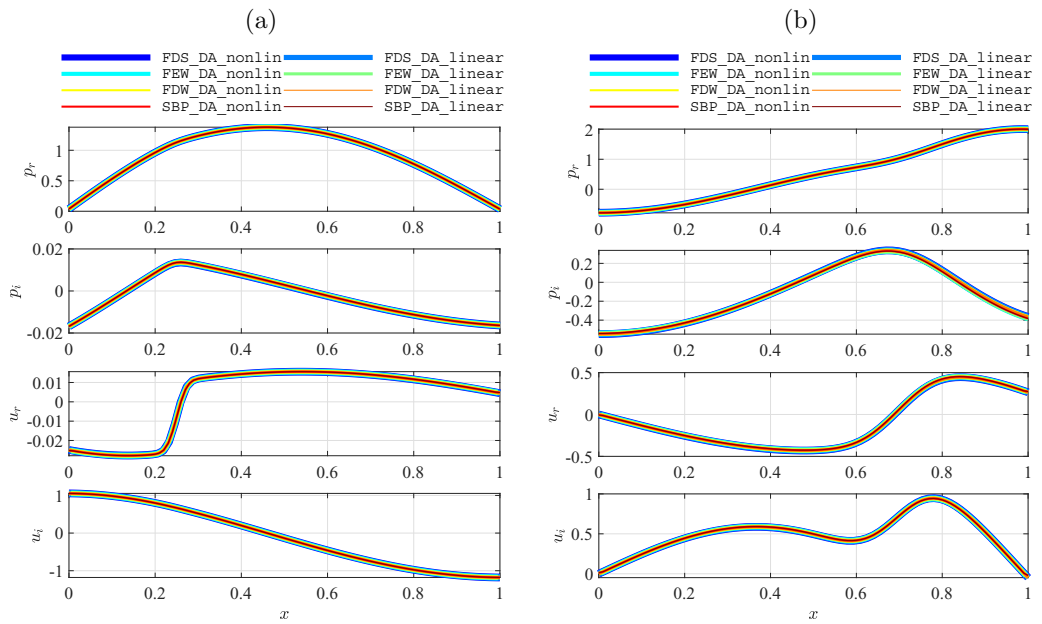

FDS_DA_nonlin	$s = 0.001936 + 3.425376\mathrm{i}$	FDS_DA_nonlin	$s = 0.461979 + 4.038162\mathrm{i}$
FDS_DA_linear	$s = 0.001936 + 3.425376\mathrm{i}$	FDS_DA_linear	$s = 0.461979 + 4.038162\mathrm{i}$
FEW_DA_nonlin	$s = 0.001926 + 3.425513\mathrm{i}$	FEW_DA_nonlin	$s = 0.461786 + 4.038140\mathrm{i}$
FEW_DA_linear	$s = 0.001926 + 3.425513\mathrm{i}$	FEW_DA_linear	$s = 0.461786 + 4.038139\mathrm{i}$
FDW_DA_nonlin	$s = 0.001936 + 3.425376\mathrm{i}$	FDW_DA_nonlin	$s = 0.461979 + 4.038162\mathrm{i}$
FDW_DA_linear	$s = 0.001936 + 3.425376\mathrm{i}$	FDW_DA_linear	$s = 0.461979 + 4.038162\mathrm{i}$
SBP_DA_nonlin	$s = 0.001924 + 3.425247\mathrm{i}$	SBP_DA_nonlin	$s = 0.461817 + 4.038056\mathrm{i}$
SBP_DA_linear	$s = 0.001924 + 3.425247\mathrm{i}$	SBP_DA_linear	$s = 0.461817 + 4.038056\mathrm{i}$

FIG. 2. Direct pressure p and velocity u eigenfunctions calculated with four different spatial discretizations (FDS, FEW, FDW, and SBP) and two iteration procedures (nonlin and linear) for the (a) Rijke tube and (b) model rocket engine, for $N = 100$. All eight lines lie on top of each other and all eigenvalues are the same to the requested tolerances. This figure was created with Fig_002.m. The agreement between the methods can be improved by increasing N.

eigenvector $\mathbf{z}$. By taking the Hermitian of (21), it is easily shown that the left eigenvectors of the direct problem $(\mathbf{A} - s^2\mathbf{C})$ are the right eigenvectors of the adjoint problem $(\mathbf{A}^H - s^{*2}\mathbf{C}^H)$. This identity can be used if a matrix eigenvalue solver does not compute the left eigenvectors automatically.

B. Discrete adjoint of the strong form (FDS_DA and SBP_DA)

The discretized form of (20) is

$$\mathbf{p}^{\dagger H}\mathbf{M}\mathbf{G}\mathbf{p} \equiv \mathbf{p}^{\dagger H}\mathbf{M}(\mathbf{A} - s^2\mathbf{C})\mathbf{p} = 0, \tag{22}$$

where $\mathbf{p}^\dagger$ contains the values of the adjoint eigenfunction $p^\dagger(x_i)$ at the collocation points and $\mathbf{M}$ is the mass matrix. In Secs. III A and III D, the discretized forms of A and C in (12) were premultiplied by $\mathbf{M}$ to create $\mathbf{A}$ and $\mathbf{C}$ in (13) and (17). This ensures that the left eigenvectors of the discretized problem, $\mathbf{z}$ in (21), are the values of the adjoint eigenfunction $p^\dagger(x_i)$ in (20) at the collocation points.

The advantage of finding the adjoint eigenfunction through this approach, which is known as the discrete adjoint approach, is that the direct and adjoint problems use the same matrices $\mathbf{A}$ and $\mathbf{C}$ and therefore contain the same discretization and truncation errors and have the same eigenvalues to machine precision. Another advantage is that the boundary conditions are already embedded within $\mathbf{A}$ and $\mathbf{C}$ and do not need to be evaluated separately. The disadvantage is that, when Neumann or Robin boundary conditions are applied by replacing rows in $\mathbf{A}$ and $\mathbf{C}$, as done for `FDS` in Sec. III A, (i) the left eigenvector takes an arbitrary value at the wall and (ii) the left eigenvector oscillates around the boundary, for as many grid points as there are in the stencil in the difference matrix $\mathbf{D}$. This disadvantage can be avoided by ensuring that the $\mathbf{A}$ matrix satisfies a summation by parts formula and that the boundary conditions are applied with the simultaneous approximation term, as described in Sec. III D for `SBP`.

The first disadvantage of the `FDS_DA` method arises because Dirichlet, Neumann, and Robin boundary conditions are imposed by replacing the bottom row of $\mathbf{A}$ with the boundary condition on p and setting the bottom right element of $\mathbf{C}$ to zero. This causes $\mathbf{C}$ to become noninvertible, which results in a right eigenvector with an infinite eigenvalue. This eigenmode is discarded. For all types of boundary condition, the bottom row of $\mathbf{A}$ can be multiplied by an arbitrary constant c_u without affecting the eigenvalues s or the right eigenvectors $\mathbf{p}$ (i.e., the thick blue lines in Fig. 2 do not depend on c_u). The arbitrary constant does, however, affect the corresponding left eigenvectors $\mathbf{z}$. For Dirichlet boundary conditions, the arbitrary constant only affects one left eigenvector: that which is discarded because it has an infinite eigenvalue. All the physical left eigenvectors are unaffected. For Neumann and Robin boundary conditions, however, every left eigenvector depends on the arbitrary constant. This can be seen in Fig. 3, which shows the adjoint eigenfunctions calculated with this method (the dark blue line) and the methods described in Secs. IV C and IV D (the remaining seven colored lines). The supplementary file `Sup_001.m` [34] plots the direct and adjoint eigenfunctions at different values of c_u. This shows that the direct eigenfunction is unaffected by c_u while the adjoint eigenfunction at the boundary is strongly affected by c_u. This problem can be anticipated by examining (20) and recalling that A contains d^2/dx^2. Therefore, if one attempts to find solutions for $p^\dagger$ and p in the same function space, the inner product is formed between two functions in different function spaces, i.e., with different numbers of degrees of freedom. In this case, this means that p can be found unambiguously, but that $p^\dagger$ can be found only up to two arbitrary constants, which in this case are c_u and c_d. This disadvantage is not serious because it does not affect the base state or feedback sensitivities (Sec. V C).

The second disadvantage of the `FDS_DA` method arises because, in $\mathbf{p}^{\dagger H}\mathbf{MG}$ in (22), the left eigenvector acts on the columns (rather than the rows) of $\mathbf{G}$. The matrix $\mathbf{G}$ contains $\mathbf{D}$, which is a difference matrix in which row i performs a difference scheme to evaluate d/dx at point i, which has a clear physical meaning. When $\mathbf{p}^{\dagger H}$ acts on column j of $\mathbf{D}$, however, the result is the sum of the contribution of point j to every difference scheme. This has no physical meaning unless a central-difference scheme is used consistently at every point, in which case $\mathbf{D}^H = \mathbf{D}$ and $\mathbf{p}^{\dagger H}$ acting on column j of $\mathbf{D}$ gives $dp^\dagger/dx$ at point j. In general, however, there is no need for the difference schemes in each row to be consistent with each other, i.e., there is no need for $\mathbf{D}$ to be Hermitian. (For example, a central-difference scheme must shift to a downwind scheme as its stencil impinges on the upstream boundary.) If the difference schemes in each row are not consistent with each other then the value of $\mathbf{p}^{\dagger H}$ acting on column j of $\mathbf{D}$ contains contributions from different difference schemes. In practice this leads to oscillations appearing in $\mathbf{p}^\dagger$ if $\mathbf{p}^\dagger$ is not zero at the boundary (i.e., when non-Dirichlet boundary conditions are applied). These oscillations occur around the boundaries for as many grid points as are in the stencil of the difference scheme. For the Chebyshev difference scheme used in this paper, $\mathbf{D}$ is a full matrix with a different difference scheme in each row. These oscillations therefore extend into the whole domain, as can be seen for `FDS_DA` in Fig. 3. Their amplitude, but not their shape, depends on the value at the boundary and therefore on c_u and c_d.

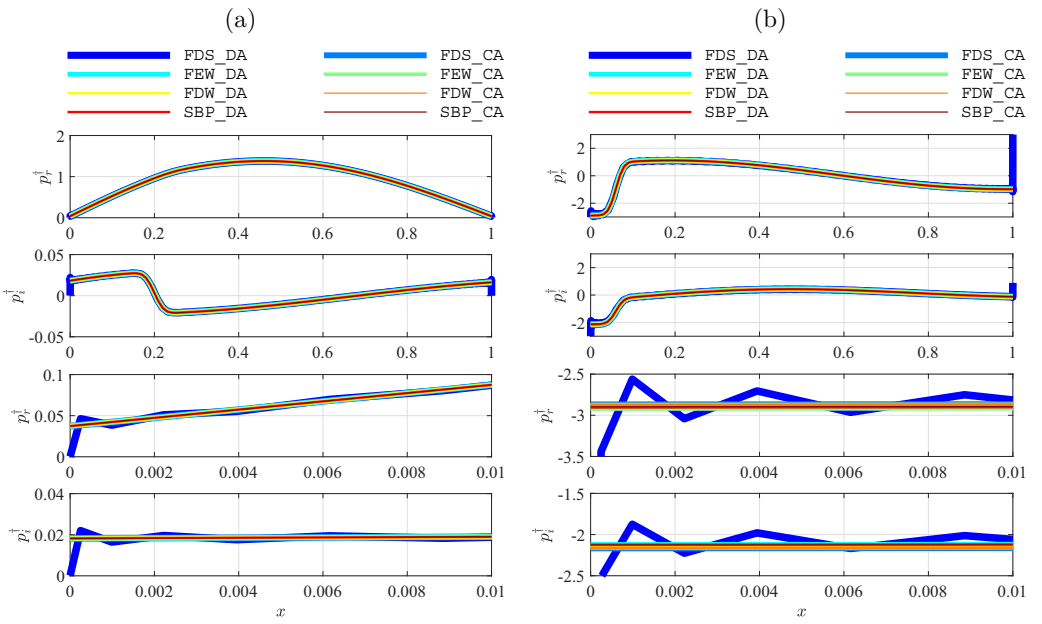

FDS_DA_nonlin	$s = 0.001936 + 3.425376\mathrm{i}$	FDS_DA_nonlin	$s = 0.461979 + 4.038162\mathrm{i}$
FDS_CA_nonlin	$s = 0.001936 - 3.425376\mathrm{i}$	FDS_CA_nonlin	$s = 0.460125 - 4.034446\mathrm{i}$
FEW_DA_nonlin	$s = 0.001926 + 3.425513\mathrm{i}$	FEW_DA_nonlin	$s = 0.461786 + 4.038139\mathrm{i}$
FEW_CA_nonlin	$s = 0.001904 - 3.425514\mathrm{i}$	FEW_CA_nonlin	$s = 0.458556 - 4.031892\mathrm{i}$
FDW_DA_nonlin	$s = 0.001936 + 3.425376\mathrm{i}$	FDW_DA_nonlin	$s = 0.461979 + 4.038162\mathrm{i}$
FDW_CA_nonlin	$s = 0.001936 - 3.425376\mathrm{i}$	FDW_CA_nonlin	$s = 0.460125 - 4.034441\mathrm{i}$
SBP_DA_nonlin	$s = 0.001924 + 3.425247\mathrm{i}$	SBP_DA_nonlin	$s = 0.461817 + 4.038056\mathrm{i}$
SBP_CA_nonlin	$s = 0.001952 - 3.425247\mathrm{i}$	SBP_CA_nonlin	$s = 0.459029 - 4.032145\mathrm{i}$

FIG. 3. Adjoint pressure $p^\dagger$ eigenfunctions calculated with four different spatial discretizations (FDS, FEW, FDW, and SBP) with either the discrete adjoint method DA or the continuous adjoint method CA for the (a) Rijke tube and (b) model rocket engine, for $N = 100$. The bottom two frames show a close-up around the boundaries, revealing oscillations in the discrete adjoint of the finite difference of the strong form equations with replacement boundary conditions (FDS_DA). For the rocket engine, the CA and DA eigenfunctions and eigenvalues differ slightly from each other because $w_{\overline{\rho}}$ is not quite zero at the boundary (order 10^{-3}), so the neglected term in (24) has a slight influence. This figure was created with Fig_003.m. By running this with larger N, one can check that the eigenvalues are the same to the requested tolerance.

C. Discrete adjoint of the weak form (FEW_DA and FDW_DA)

The continuous equations (12) can be integrated by parts once to give the weak form (14). When discretized, this becomes (15) and (16). The left eigenvectors of (15a) and (16a), $\mathbf{z}$, are the adjoint eigenfunctions $p^\dagger(x_i)$ evaluated at the collocation points x_i. These are arranged in the column vector $\mathbf{p}^\dagger$. This approach has all the advantages of the discrete adjoint in the strong form but does not have its disadvantages. First, this is because $\mathbf{p}^\dagger$ acts on $\mathbf{D}^H$, rather than $\mathbf{D}$. Second, this is because s, $\mathbf{p}$, and $\mathbf{p}^\dagger$ are defined uniquely, without involving any arbitrary constants. (An arbitrary constant is involved in imposing Dirichlet boundary conditions but this only affects the discarded eigenmode.) Alternatively, this outcome can be anticipated by examining (14) and noting that each inner product is between functions that exist in the same function space. This means that $p^\dagger$ and p can be found unambiguously, without involving arbitrary constants.

D. Continuous adjoint in the strong form

Having defined the adjoint eigenfunction in (20), the test function z in (14) is now replaced with the adjoint eigenfunction $p^\dagger$ and Eq. (14) is integrated by parts a second time to give the strong form of the continuous adjoint equations

$$\langle p^\dagger, (A - s^2 C)p\rangle = \left[p^{\dagger *}\overline{v}\frac{dp}{dx} - \overline{v}\frac{dp^{\dagger *}}{dx}p - w_{\overline{\rho}}\langle p^\dagger, \zeta n(e^{-s\tau})h\rangle p \right]_0^1 + \langle (A^\dagger - s^{*2}C^\dagger)p^\dagger, p\rangle = 0, \tag{23a}$$

where

$$A^\dagger p^\dagger \equiv \frac{d}{dx}\left(\overline{v}^*\frac{dp^\dagger}{dx}\right) + \left(\frac{dw^*_{\overline{\rho}}}{dx}\right)\langle \zeta n(e^{-s\tau})h, p^\dagger\rangle, \tag{23b}$$

$$C^\dagger \equiv 1/\gamma^*. \tag{23c}$$

Equation (23) must be satisfied for arbitrary p. The inner product term in (23a) provides the continuous adjoint equations $(A^\dagger - s^{*2}C^\dagger)p^\dagger = 0$. The eigenvalue of the adjoint problem is the complex conjugate of that of the direct problem. The boundary term in (23a) provides the boundary conditions for the adjoint eigenfunction $p^\dagger$ in terms of those for the direct eigenfunction p. For homogeneous Dirichlet boundary conditions on p, the boundary term requires homogeneous Dirichlet boundary conditions on $p^\dagger$, by inspection. For Robin boundary conditions $dp/dx = kp$, each boundary must satisfy

$$p^{\dagger *}\overline{v}k - \overline{v}\frac{dp^{\dagger *}}{dx} - w_{\overline{\rho}}\langle p^\dagger, \zeta n(e^{-s\tau})h\rangle = 0. \tag{24}$$

If the measurement function $w_{\overline{\rho}}$ smoothly tends to zero at the boundary then this simply requires $dp^\dagger/dx = k^* p^\dagger$, which are Robin boundary conditions on $p^\dagger$. However, if $w_{\overline{\rho}}$ does not smoothly tend to zero at the boundary then the boundary condition on $p^\dagger$ requires information about $p^\dagger$ in the entire domain, through the inner product $\langle p^\dagger, \zeta n(e^{-s\tau})h\rangle$. Solving this is difficult and it is therefore wise to move the boundary to ensure that $w_{\overline{\rho}}$ smoothly tends to zero at the boundary. (This effect can be seen particularly clearly by comparing the `CA` and `DA` eigenvalues for the model rocket when the measurement location X_w is moved close to the inlet.)

The continuous approach has the advantage that the adjoint eigenfunction $p^\dagger$ can unambiguously be calculated in the same function space as the direct eigenfunction p without the use of arbitrary constants. It has two slight disadvantages. First, the boundary conditions have to be evaluated and implemented separately, which can be challenging and error prone. Second, the direct and adjoint problems can have different discretizations, different truncation errors, and different solution algorithms. This means that the direct and adjoint eigenvalues are not identical to machine precision. This precludes the use of stringent convergence tests to debug the continuous adjoint code (Sec. V F). It may be convenient to write a discrete adjoint code in order to debug a continuous adjoint code, which was the approach taken in [35].

The continuous approach also provides a physical interpretation of the adjoint variable. The heat release term of the direct equation (12b) can be integrated by parts once to give

$$Ap = \frac{d}{dx}\left(\overline{v}\frac{dp}{dx}\right) + \zeta n(e^{-s\tau})h\left\langle \frac{dw^*_{\overline{\rho}}}{dx}, p\right\rangle \tag{25}$$

if, as is likely, $h = 0$ at the boundaries. The acoustic terms (the first terms) in (23b) and (25) are the same. This is expected because acoustic equations are self-adjoint in the absence of damping and forcing. The heat release terms (the second terms) in (23b) and (25) are mirror images of each other. In the direct equation (25), the amplitude of the forcing is determined by the integral of the pressure and the gradient of the measurement function $w'_{\overline{\rho}}$, while its position is determined by the heat release function $(e^{-s\tau})h(x)$. In brief, this term is influenced by the measurement region and influences the

heat release region. In the adjoint equation (23b), the amplitude of the forcing is determined by the integral of the adjoint pressure and heat release function, while its position is determined by the gradient of the measurement function. In brief, this term is influenced by the heat release region and influences the measurement region. This shows that the system becomes more non-self-adjoint the more that $(e^{-s\tau})h$ differs from $w'_{\overline{\rho}}$. This difference is caused by the spatial separation of the peaks of $h(x)$ and $w(x)$, and the time delay $\tau(x)$. This has physical implications (Sec. VIII). Note also that if the measurement region is a Dirac δ, $w(x) = \delta(x - x_{\text{ref}})$, as is often the case in practical implementations, then the heat release term in the above adjoint equation contains the derivative of a Dirac δ. It is then advisable to integrate this term by parts so that this becomes the evaluation of dp/dx at x_w. In this paper, x_w is expanded to a measurement region in order to avoid this.

E. Implementation of the continuous adjoint equations `*_CA`

A column vector $\mathbf{w}'_{\overline{\rho}}$ is defined to contain $dw_{\overline{\rho}}/dx$ at the collocation points. The discretized forms of (23) are

$$\mathbf{G}^\dagger(s)\mathbf{p}^\dagger \equiv (\mathbf{A}^\dagger(s) - s^{*2}\mathbf{C}^\dagger)\mathbf{p}^\dagger = 0, \tag{26}$$

where, for the finite difference of the strong form (`mat_AC_FDS_CA.m`),

$$\mathbf{A}^\dagger \equiv \mathbf{MDVD} + \mathbf{M}\zeta n\mathbf{w}'_{\overline{\rho}}\mathbf{h}^H(\mathbf{e}^{-s^*\tau^*})\mathbf{M}, \tag{27a}$$

$$\mathbf{C}^\dagger \equiv \mathbf{M}/\gamma; \tag{27b}$$

for the finite element of the weak form (`mat_AC_FEW_CA.m`),

$$\mathbf{A}^\dagger_{11} \equiv -\mathbf{D}^H_{01}\mathbf{M}_{00}\mathbf{V}_{00}\mathbf{D}_{01} + \mathbf{M}_{11}\zeta n\mathbf{w}'_{\overline{\rho}1}\mathbf{h}^H_1(\mathbf{e}^{-s^*\tau^*_1})\mathbf{M}_{11}, \tag{28a}$$

$$\mathbf{C}^\dagger_{11} \equiv \mathbf{M}_{11}/\gamma; \tag{28b}$$

for the finite difference of the weak form (`mat_AC_FDW_CA.m`),

$$\mathbf{A}^\dagger \equiv -\mathbf{D}^H\mathbf{MVD} + \mathbf{M}\zeta n\mathbf{w}'_{\overline{\rho}}\mathbf{h}^H(\mathbf{e}^{-s^*\tau^*})\mathbf{M}, \tag{29a}$$

$$\mathbf{C}^\dagger \equiv \mathbf{M}/\gamma; \tag{29b}$$

and for the finite difference of the strong form obeying a summation by parts formula and with the simultaneous approximation term (`mat_AC_SBP_CA.m`),

$$\mathbf{A}^\dagger \equiv -\mathbf{D}^H_{01}\mathbf{M}_{00}\mathbf{V}_{00}\mathbf{D}_{01} + \tilde{\mathbf{V}}\mathbf{S} + \mathbf{M}\zeta n\mathbf{w}'_{\overline{\rho}}\mathbf{h}^H(\mathbf{e}^{-s^*\tau^*})\mathbf{M}, \tag{30a}$$

$$\mathbf{C}^\dagger \equiv \mathbf{M}/\gamma. \tag{30b}$$

The boundary conditions are applied in the same way as for the direct equations, but with the complex conjugates of k_u and k_d for Robin boundary conditions.

F. Iteration procedures

For the discretized direct systems (13)–(17), the left eigenvector $\mathbf{z}$ in (21) contains the values of the adjoint eigenfunction at the grid points $p^\dagger(x_i)$ in (20) as explained in Secs. IV B and IV C. For the Newton method, this left eigenvector is found by calculating the null space of $\mathbf{G}^H$. For the active iteration method, this left eigenvector is calculated alongside the right eigenvector using `fun_eig_nearest`.

For the continuous adjoint equations (27)–(30), solutions are found in the same ways as for the direct problem: (i) the Newton method applied to the nonlinear eigenvalue problem $|\mathbf{G}^\dagger(s)| = 0$ and (ii) the active iteration method applied to the sequence of linear eigenvalue problems $\mathbf{A}^\dagger(s_{j-1})\mathbf{p}^\dagger = s_j^{*2}\mathbf{C}^\dagger\mathbf{p}^\dagger$. In each case, the values of the adjoint eigenfunction at the grid points $p^\dagger(x_i)$ in (20) are the components of the right eigenvector $\mathbf{p}^\dagger$.

G. Results

Figure 3 shows the adjoint eigenfunctions calculated with the discrete (DA) and continuous (CA) adjoint approaches for the finite difference in the strong form (FDS), the finite element (FEW), the finite difference in the weak form (FDW), and the summation by parts finite difference (SBP). For presentation, they have been normalized such that $\int_0^1 {p^\dagger}^2 dx = 1$. From a computational point of view, the main point is that all the methods give the same results but the discrete adjoint of the finite difference of the strong form (FDS_DA) gives arbitrary values at the boundary and oscillations around the boundary, as described in Sec. IV B. From a physical point of view, Fig. 3 shows that the adjoint pressure eigenfunction $p^\dagger$ changes abruptly at the measurement region, while the direct pressure and velocity eigenfunctions p and u in Fig. 2 change at the heat release region. These features can be anticipated by comparing (23b) with (25) and show clearly that the problem is not self-adjoint. The adjoint eigenfunctions are used to calculate the base state sensitivities (Sec. V), the feedback sensitivities (Sec. VI), and the receptivities (Sec. VII).

V. BASE STATE SENSITIVITY ANALYSIS

In this section, the theory and numerics of the base state sensitivity analysis is described for the continuous framework (Sec. V A) and the discrete framework (Sec. V B) in the FDS, FEW, FDW, and SBP formulations. The physical interpretation of the base state sensitivities is in Sec. VIII C.

A. Base state sensitivities in the continuous framework

The direct equation (12) is an eigenvalue problem $G(s)p = 0$, possibly with boundary conditions that depend on s. If the operator $G(s)$ is perturbed to $G + \epsilon\delta G$ then each eigenvalue shifts to $s + \epsilon\delta s$ and its corresponding direct eigenfunction to $p + \epsilon\delta p$. The governing equations must still be satisfied, so

$$\left(G(s) + \epsilon\delta s\frac{dG}{ds} + \epsilon\delta G\right)(p + \epsilon\delta p) + O(\epsilon^2) = 0. \tag{31}$$

This is correct for nondegenerate eigenvalues. The sensitivity of degenerate eigenvalues requires a different approach [36]. Considering terms at order ϵ gives

$$G\delta p + \delta s\frac{dG}{ds}p + (\delta G)p = 0. \tag{32}$$

Using the inner product (11), this expression is premultiplied by the corresponding adjoint eigenfunction, which is defined such that $\langle p^\dagger, Gf\rangle = 0$ for any f, and rearranged to

$$\delta s = \frac{\langle p^\dagger, (\delta G)p\rangle}{\alpha}, \tag{33a}$$

where

$$\alpha \equiv \left\langle p^\dagger, -\frac{dG}{ds}p\right\rangle = \left\langle p^\dagger, -\left(\left.\frac{\partial G}{\partial s}\right|_k + \frac{dk}{ds}\left.\frac{\partial G}{\partial k}\right|_s\right)p\right\rangle. \tag{33b}$$

The final term in (33b) accounts explicitly for frequency-dependent Robin boundary conditions. From (12), $\partial G/\partial s|_k = \zeta n(\tau e^{-s\tau})h\langle w_\rho^*, d/dx\rangle - 2sC$. In order to make k appear explicitly in (33b), the equation is integrated by parts to obtain $(dk/ds) \times (\partial/\partial k)$ of (14). Then dp/dx in the boundary term is replaced with kp. Then this is differentiated with respect to k. If $w_{\overline{\rho}}^* = 0$ at the boundaries, which is good practice because of (24), the final expression for α is

$$\alpha = -\left\langle p^\dagger, \zeta n(\tau e^{-s\tau})h\left\langle w_\rho^*, \frac{dp}{dx}\right\rangle - 2sC\right\rangle - {p^\dagger}_u\overline{v}_u\frac{dk_u}{ds}p_u - {p^\dagger}_d\overline{v}_d\frac{dk_d}{ds}p_d, \tag{34}$$

where the final two terms are required only for frequency-dependent Robin boundary conditions.

The numerator of (33a) is considered next. The operator G depends on the base state variables $\overline{v}(x)$, n, $\tau(x)$, $h(x)$, and $w_{\overline{\rho}}(x)$, described generically as $b(x)$, and the Robin boundary conditions k_u and k_d, described generically as k. If these base state variables are each perturbed by ϵ then the numerator of (33) is found by setting $z = p^\dagger$ in (14) and perturbing each base state variable to give

$$\begin{aligned}\langle p^\dagger, (\delta G)p\rangle = &+ p^{\dagger *}_d(\delta\overline{v}_d)k_d p_d + p^{\dagger *}_d\overline{v}_d(\delta k_d)p_d + p^{\dagger *}_u(\delta\overline{v}_u)k_u p_u + p^{\dagger *}_u\overline{v}_u(\delta k_u)p_u \\ &- \left\langle \frac{dp^\dagger}{dx}, (\delta\overline{v})\frac{dp}{dx}\right\rangle - \left\langle p^\dagger, \zeta(\delta n)(e^{-s\tau})h\left\langle w^*_{\overline{\rho}}, \frac{dp}{dx}\right\rangle\right\rangle \\ &- \left\langle p^\dagger, \zeta n(-s(\delta\tau)e^{-s\tau})h\left\langle w^*_{\overline{\rho}}, \frac{dp}{dx}\right\rangle\right\rangle - \left\langle p^\dagger, \zeta n(e^{-s\tau})(\delta h)\left\langle w^*_{\overline{\rho}}, \frac{dp}{dx}\right\rangle\right\rangle \\ &- \left\langle p^\dagger, \zeta n(e^{-s\tau})h\left\langle (\delta w^*_{\overline{\rho}}), \frac{dp}{dx}\right\rangle\right\rangle. \end{aligned} \tag{35}$$

(Note that the upstream boundary terms are positive because the upstream surface normal points in the negative x direction.) If the base state perturbation δb or δk is known *a priori* then the eigenvalue shift δs is found by substituting δb or δk into (35). If the base state perturbation is not known *a priori* then it is useful instead to define the sensitivities $\partial s/\partial k$ and $\partial s/\partial b(x)$ such that

$$\frac{\partial s}{\partial k}\delta k \equiv \epsilon \lim_{\epsilon \to 0} \frac{s(k+\epsilon\delta k) - s(k)}{\epsilon} \equiv \delta s, \tag{36}$$

$$\int_0^1 \frac{\partial s}{\partial b}(x)\delta b(x)dx \equiv \epsilon \lim_{\epsilon \to 0} \frac{s(b(x)+\epsilon\delta b(x)) - s(b(x))}{\epsilon} \equiv \delta s. \tag{37}$$

These sensitivities give the influence of δk at the boundary and $\delta b(x)$ at every point in space. They are defined without complex conjugation, unlike the inner product (11), so the corresponding MATLAB code is easier to read. Equating (36) and (37) with the relevant terms in (35) leads to the algebraic expressions for the base state sensitivities in the top left quadrant of Table II. This process also gives the sensitivity to local density changes at the boundary, but this has little relevance and is not recorded here. These sensitivities are calculated with the MATLAB code `fun_ds_CA.m` and are the same for all four discretizations. They are shown in Fig. 4 for the four discretizations (`FDS_CA`, `FEW_CA`, `FDW_CA`, and `SBP_CA`).

B. Base state sensitivities in the discrete framework

In the discrete framework, all boundary conditions are embedded within the matrix $\mathbf{G}$ and so do not need to be considered separately. An analysis similar to (31) and (32), but for matrices with left and right eigenvectors $\mathbf{p}^\dagger$ and $\mathbf{p}$, gives

$$\delta s = \frac{\mathbf{p}^{\dagger H}\delta\mathbf{G}\mathbf{p}}{\alpha} \tag{38}$$

where

$$\alpha \equiv \mathbf{p}^{\dagger H}\left(\frac{d\mathbf{G}}{ds}\right)\mathbf{p}.$$

In the discrete framework the base state perturbation is a column vector $\delta\mathbf{b}$ and the sensitivity of s is defined as the row vector $\partial s/\partial\mathbf{b}$ such that

$$\delta s = (\partial s/\partial\mathbf{b})\delta\mathbf{b}. \tag{39}$$

For the discretized equations in the strong form (13), the sensitivities with respect to the base state variables are given in the top right quadrant of Table II and are coded into `mat_AC_FDS_DA.m`.

TABLE II. Base state sensitivities derived in the continuous framework (33), discretized strong form, discretized weak form, and SBP SAT discretized strong form. The inner product α is defined in (33b) and (38). Expressions within curly brackets $\{\circ\}$ and the inner product $\langle\circ,\circ\rangle$ are numbers. Expressions within parentheses $(\circ)$ or square brackets $[\circ]$ are functions of x in the continuous framework and row vectors in the discrete frameworks. The symbol $\odot$ denotes element by element multiplication of two row vectors.

Base state sensitivity	Continuous (`*_CA`)	Discretized strong form (`FDS_DA`)
$\{\partial s/\partial k_u\}$	$p^{\dagger *}_u \overline{v}_u p_u/\alpha$	$\mathbf{p}^{\dagger *}_u c_u \mathbf{p}_u/\alpha$
$\{\partial s/\partial k_d\}$	$p^{\dagger *}_d \overline{v}_d p_d/\alpha$	$-\mathbf{p}^{\dagger *}_d c_d \mathbf{p}_d/\alpha$
$(\partial s/\partial \overline{v})$	$-(\frac{dp^\dagger}{dx})^*(\frac{dp}{dx})/\alpha$	$(\mathbf{p}^{\dagger H}\mathbf{M}\mathbf{D})\odot(\mathbf{D}\mathbf{p})^T/\alpha$
$\{\partial s/\partial n\}$	$-\langle p^{\dagger *},\zeta(e^{-s\tau})h\rangle\langle w^*_{\overline{\rho}},\frac{dp}{dx}\rangle/\alpha$	$-\{\mathbf{p}^{\dagger H}\mathbf{M}\zeta(\mathbf{e}^{-s\tau})\mathbf{h}\}\times\{\mathbf{w}^T_{\overline{\rho}}\mathbf{M}\mathbf{D}\mathbf{p}\}/\alpha$
$(\partial s/\partial \tau)$	$(p^{\dagger *})[\zeta n s(e^{-s\tau})h]\langle w^*_{\overline{\rho}},\frac{dp}{dx}\rangle/\alpha$	$(\mathbf{p}^{\dagger H}\mathbf{M})\odot[\zeta n s(\mathbf{e}^{-s\tau})\mathbf{h}]^T\times\{\mathbf{w}^T_{\overline{\rho}}\mathbf{M}\mathbf{D}\mathbf{p}\}/\alpha$
$(\partial s/\partial h)$	$-(p^{\dagger *})[\zeta n(e^{-s\tau})]\langle w^*_{\overline{\rho}},\frac{dp}{dx}\rangle/\alpha$	$-[\mathbf{p}^{\dagger H}\mathbf{M}\zeta n(\mathbf{e}^{-s\tau})]\times\{\mathbf{w}^T_{\overline{\rho}}\mathbf{M}\mathbf{D}\mathbf{p}\}/\alpha$
$(\partial s/\partial w^*_{\overline{\rho}})$	$-\langle p^{\dagger *},\zeta n(e^{-s\tau})h\rangle(\frac{dp}{dx})/\alpha$	$-\{\mathbf{p}^{\dagger H}\mathbf{M}\zeta n(\mathbf{e}^{-s\tau})\mathbf{h}\}\times(\mathbf{M}\mathbf{D}\mathbf{p})^T/\alpha$
Base state sensitivity	Discretized weak form (`FEW_DA` and `FDW_DA`)	SBP SAT (`SBP_DA`)
$\{\partial s/\partial k_u\}$	$\mathbf{p}^{\dagger *}_u \overline{v}_u \mathbf{p}_u/\alpha$	$\mathbf{p}^{\dagger *}_u \overline{v}_u \mathbf{p}_u/\alpha$
$\{\partial s/\partial k_d\}$	$\mathbf{p}^{\dagger *}_d \overline{v}_d \mathbf{p}_d/\alpha$	$\mathbf{p}^{\dagger *}_d \overline{v}_d \mathbf{p}_d/\alpha$
$(\partial s/\partial \overline{v})$	$-(\mathbf{p}^{\dagger H}_1\mathbf{D}^H_{01}\mathbf{M}_{00})\odot(\mathbf{D}_{01}\mathbf{p}_1)^T/\alpha$	$-(\mathbf{p}^{\dagger H}\mathbf{D}^H_{01}\mathbf{M}_{00})\odot(\mathbf{D}_{01}\mathbf{p})^T/\alpha$
$\{\partial s/\partial n\}$	$-\{\mathbf{p}^{\dagger H}_1\mathbf{M}_{11}\zeta(\mathbf{e}^{-s\tau_1})\mathbf{h}_1\}\times\{\mathbf{w}^T_{\overline{\rho}0}\mathbf{M}_{00}\mathbf{D}_{01}\mathbf{p}\}/\alpha$	$-\{\mathbf{p}^{\dagger H}\mathbf{M}\zeta(\mathbf{e}^{-s\tau})\mathbf{h}\}\times\{\mathbf{w}^T_{\overline{\rho}}\mathbf{M}\mathbf{D}_1\mathbf{p}\}/\alpha$
$(\partial s/\partial \tau)$	$(\mathbf{p}^{\dagger H}_1\mathbf{M}_{11})\odot[\zeta n s(\mathbf{e}^{-s\tau_1})\mathbf{h}_1]^T\times\{\mathbf{w}^T_{\overline{\rho}0}\mathbf{M}_{00}\mathbf{D}_{01}\mathbf{p}_1\}/\alpha$	$(\mathbf{p}^{\dagger H}\mathbf{M})\odot[\zeta n s(\mathbf{e}^{-s\tau})\mathbf{h}]^T\times\{\mathbf{w}^T_{\overline{\rho}}\mathbf{M}\mathbf{D}_1\mathbf{p}\}/\alpha$
$(\partial s/\partial h)$	$-[\mathbf{p}^{\dagger H}_1\mathbf{M}_{11}\zeta n(\mathbf{e}^{-s\tau_1})]\times\{\mathbf{w}^T_{\overline{\rho}0}\mathbf{M}_{00}\mathbf{D}_{01}\mathbf{p}_1\}/\alpha$	$-[\mathbf{p}^{\dagger H}\mathbf{M}\zeta n(\mathbf{e}^{-s\tau})]\times\{\mathbf{w}^T_{\overline{\rho}}\mathbf{M}\mathbf{D}_1\mathbf{p}\}/\alpha$
$(\partial s/\partial w^*_{\overline{\rho}})$	$-\{\mathbf{p}^{\dagger H}_1\mathbf{M}_{11}\zeta n(\mathbf{e}^{-s\tau_1})\mathbf{h}_1\}\times(\mathbf{M}_{00}\mathbf{D}_{01}\mathbf{p}_1)^T/\alpha$	$-\{\mathbf{p}^{\dagger H}\mathbf{M}\zeta n(\mathbf{e}^{-s\tau})\mathbf{h}\}\times(\mathbf{M}\mathbf{D}_1\mathbf{p})^T/\alpha$

For the discretized equations in the weak form (15), the sensitivities with respect to the base state variables are given in the bottom left quadrant of Table II and are coded into `mat_AC_FEW_DA.m` and `mat_AC_FDW_DA.m`. For the discretized equations in the strong form using a summation by parts formula with a simultaneous approximation term, the sensitivities are given in the bottom right quadrant of Table II and are coded into `mat_AC_SBP_DA.m`. They are plotted in Fig. 4.

In the finite-element framework, the base state sensitivities are the same types of function as their respective base state variable. Therefore, $\partial s/\partial \mathbf{h}_1$ and $\partial s/\partial \tau_1$ are P1 while $\partial s/\partial \mathbf{w}_{\overline{\rho}0}$ and $\partial s/\partial \mathbf{v}_0$ are P0. For the weak form equations and the strong form equations in SBP SAT form, $\overline{v}_u k_u$ is added to the bottom right element and $\overline{v}_d k_d$ is added to the top left element of $\mathbf{A}$. The corresponding sensitivities to k_u and k_d are given in Table II. For the strong form equations with replacement boundary conditions, a Robin upstream boundary condition is imposed by replacing the bottom row of $\mathbf{A}$ with the bottom row of $\mathbf{D}$, then adding k_u to the bottom right element, and multiplying the whole row by an arbitrary constant c_u. For the downstream boundary condition, a similar procedure is used but k_d is subtracted from the top left element and the arbitrary constant is c_d. The inclusion of c_u and c_d in $\partial s/\partial k_u$ and $\partial s/\partial k_d$ means that $\partial s/\partial k_u$ and $\partial s/\partial k_d$ are calculated exactly (as shown in Fig. 4), even though the boundary values of the left eigenvector $\mathbf{p}^\dagger{}_u$ and $\mathbf{p}^\dagger{}_d$ depend on the arbitrary constants c_u and c_d.

C. Problems with the base state sensitivities in the discrete strong form

Examination of the expressions in Table II reveals subtle features of the sensitivities derived from the discretized strong form equations with replacement boundary conditions `FDS_DA`. The first feature is that, although $\delta\overline{\mathbf{v}}$ and $\delta\mathbf{w}_{\overline{\rho}}$ contain $N+1$ independent elements, their corresponding sensitivities $\partial s/\partial\overline{\mathbf{v}}$ and $\partial s/\partial\mathbf{w}_{\overline{\rho}}$ contain only N independent elements. This can be seen in Table II:

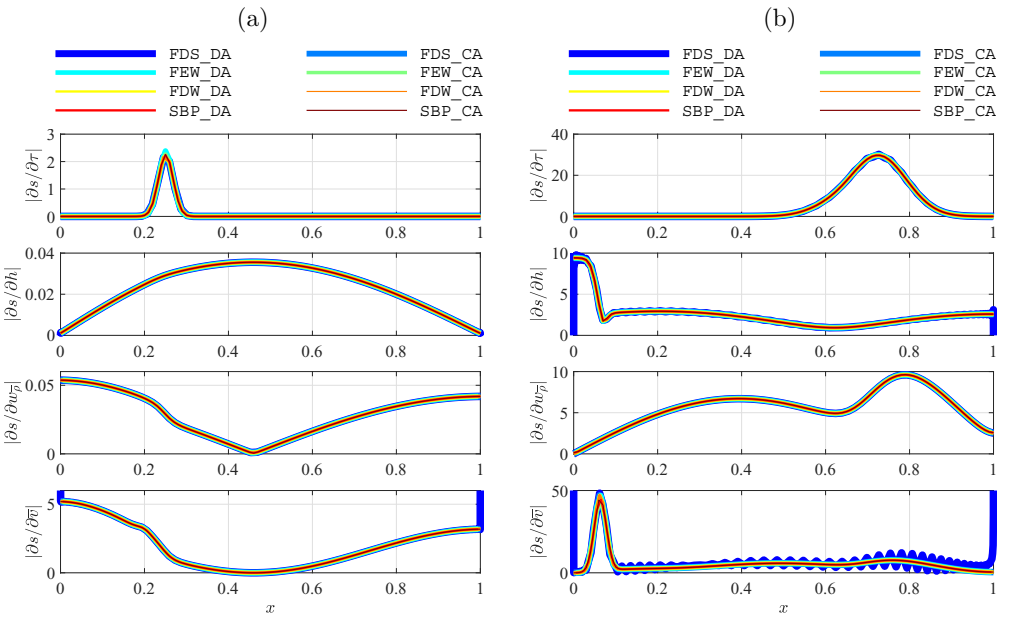

	(a)	(b)
FDS_DA	$\partial s/\partial n = +0.178439 - 0.023278\mathrm{i}$	$\partial s/\partial n = +0.018691 + 0.022693\mathrm{i}$
FDS_CA	$\partial s/\partial n = +0.178439 - 0.023278\mathrm{i}$	$\partial s/\partial n = +0.018715 + 0.022716\mathrm{i}$
FEW_DA	$\partial s/\partial n = +0.178385 - 0.023319\mathrm{i}$	$\partial s/\partial n = +0.018677 + 0.022686\mathrm{i}$
FEW_CA	$\partial s/\partial n = +0.178382 - 0.023338\mathrm{i}$	$\partial s/\partial n = +0.018712 + 0.022723\mathrm{i}$
FDW_DA	$\partial s/\partial n = +0.178439 - 0.023278\mathrm{i}$	$\partial s/\partial n = +0.018691 + 0.022693\mathrm{i}$
FDW_CA	$\partial s/\partial n = +0.178439 - 0.023278\mathrm{i}$	$\partial s/\partial n = +0.018715 + 0.022716\mathrm{i}$
SBP_DA	$\partial s/\partial n = +0.178323 - 0.023277\mathrm{i}$	$\partial s/\partial n = +0.018688 + 0.022698\mathrm{i}$
SBP_CA	$\partial s/\partial n = +0.178327 - 0.023253\mathrm{i}$	$\partial s/\partial n = +0.018735 + 0.022736\mathrm{i}$
FDS_DA	$\partial s/\partial k_u = +0.000553 - 0.000668\mathrm{i}$	$\partial s/\partial k_u = -2.984076 + 2.894226\mathrm{i}$
FDS_CA	$\partial s/\partial k_u = +0.000553 - 0.000668\mathrm{i}$	$\partial s/\partial k_u = -2.983423 + 2.891128\mathrm{i}$
FEW_DA	$\partial s/\partial k_u = +0.000553 - 0.000668\mathrm{i}$	$\partial s/\partial k_u = -2.983221 + 2.892682\mathrm{i}$
FEW_CA	$\partial s/\partial k_u = +0.000553 - 0.000668\mathrm{i}$	$\partial s/\partial k_u = -2.981437 + 2.885780\mathrm{i}$
FDW_DA	$\partial s/\partial k_u = +0.000553 - 0.000668\mathrm{i}$	$\partial s/\partial k_u = -2.984076 + 2.894225\mathrm{i}$
FDW_CA	$\partial s/\partial k_u = +0.000553 - 0.000668\mathrm{i}$	$\partial s/\partial k_u = -2.983415 + 2.891133\mathrm{i}$
SBP_DA	$\partial s/\partial k_u = +0.000553 - 0.000668\mathrm{i}$	$\partial s/\partial k_u = -2.985267 + 2.894484\mathrm{i}$
SBP_CA	$\partial s/\partial k_u = +0.000553 - 0.000668\mathrm{i}$	$\partial s/\partial k_u = -2.985075 + 2.891926\mathrm{i}$
FDS_DA	$\partial s/\partial k_d = +0.000702 - 0.000839\mathrm{i}$	$\partial s/\partial k_d = +1.201426 - 2.116687\mathrm{i}$
FDS_CA	$\partial s/\partial k_d = +0.000702 - 0.000839\mathrm{i}$	$\partial s/\partial k_d = +1.204851 - 2.113137\mathrm{i}$
FEW_DA	$\partial s/\partial k_d = +0.000702 - 0.000839\mathrm{i}$	$\partial s/\partial k_d = +1.202273 - 2.115615\mathrm{i}$
FEW_CA	$\partial s/\partial k_d = +0.000702 - 0.000839\mathrm{i}$	$\partial s/\partial k_d = +1.208283 - 2.109138\mathrm{i}$
FDW_DA	$\partial s/\partial k_d = +0.000702 - 0.000839\mathrm{i}$	$\partial s/\partial k_d = +1.201426 - 2.116687\mathrm{i}$
FDW_CA	$\partial s/\partial k_d = +0.000702 - 0.000839\mathrm{i}$	$\partial s/\partial k_d = +1.204850 - 2.113128\mathrm{i}$
SBP_DA	$\partial s/\partial k_d = +0.000702 - 0.000838\mathrm{i}$	$\partial s/\partial k_d = +1.201761 - 2.117325\mathrm{i}$
SBP_CA	$\partial s/\partial k_d = +0.000702 - 0.000838\mathrm{i}$	$\partial s/\partial k_d = +1.206799 - 2.112346\mathrm{i}$

FIG. 4. Absolute values of the base state sensitivities ($\partial s/\partial \tau$, $\partial s/\partial h$, $\partial s/\partial w_{\bar{\rho}}$, $\partial s/\partial \bar{v}$, $\partial s/\partial n$, $\partial s/\partial k_u$, and $\partial s/\partial k_d$) calculated with the discrete adjoint method (DA) and continuous adjoint method (CA) for four spatial discretizations (FDS, FEW, FDW, and SBP) and for the (a) Rijke tube and (b) model rocket engine, for $N = 100$. All lines except FDS_DA lie on top of each other and all sensitivities to n, k_u, and k_d are the same to the requested precision. This figure was created with Fig_004.m. Higher precision can be achieved by increasing N.

The matrix $\mathbf{D}$ represents d/dx and therefore has rank N, meaning that $\partial s/\partial \overline{\mathbf{v}}$ is element by element multiplication of two row vectors containing N independent elements and $\partial s/\partial \mathbf{w}_{\overline{\rho}}$ is the product of a scalar with a vector $(\mathbf{MDp})^T$ containing N independent elements. This does not cause any problems and is analogous to the fact that, in the finite-element formulation, $\partial s/\partial \overline{\mathbf{v}}_0$ and $\partial s/\partial \mathbf{w}_{\overline{\rho}0}$ are P0 functions.

The second feature is due to the fact that, for non-Dirichlet boundary conditions in the `FDS_DA` framework, the left eigenvector $\mathbf{p}^\dagger$ oscillates, as explained in Sec. IV B and shown in the bottom frames of Fig. 3. For $\partial s/\partial \tau$, $\partial s/\partial \mathbf{h}$, and $\partial s/\partial \overline{\mathbf{v}}$, which contain $\mathbf{p}^\dagger$ outside an inner product, these oscillations propagate into the sensitivities. The dependence on c_u and c_d disappears, however, because they appear in both the numerator and denominator of (38). The supplementary file `Sup_002.m` [34] plots the `FDS_DA` base state sensitivities at different values of c_u, confirming that the oscillations persist but do not depend on c_u. These oscillations do not appear in $\partial s/\partial \mathbf{w}_{\overline{\rho}}$, because, for this sensitivity, $\mathbf{p}^\dagger$ is multiplied by $\mathbf{h}$ within an inner product and is then applied equally to every point in space.

The third feature is an extension of the second and is due to ${\mathbf{p}^\dagger}^H\mathbf{MD}$ in the $\partial s/\partial \overline{\mathbf{v}}$ term. For reasons described in Sec. IV B, the action of ${\mathbf{p}^\dagger}^H$ on $\mathbf{D}$ for non-Dirichlet boundary conditions creates oscillations in $\partial s/\partial \overline{\mathbf{v}}$. The fourth feature is due to the way that the boundary conditions are implemented in `FDS`. The top and bottom rows of $\mathbf{A}$ are replaced with the boundary conditions, which removes the influence of the boundary values of $\mathbf{h}$ and τ and forces the corresponding sensitivity to be zero at the boundaries. These problems can all be avoided by using the continuous adjoint method, the discretized strong SBP SAT form, or one of the discretized weak form methods.

D. Relationship between the continuous and the discrete frameworks

In the continuous framework (37) the sensitivity $\partial s/\partial b$ is calculated with respect to variations in a continuous function δb. In the discrete framework (39) the sensitivity $\partial s/\partial \mathbf{b}$ is calculated with respect to variations at a grid point $\delta \mathbf{b}$. The two are related by equating (37) with (39): $\delta s = \int (\partial s/\partial b)\delta b\, dx = (\partial s/\partial \mathbf{b})\delta \mathbf{b}$. If $(\partial s/\partial \mathbf{b})_{\text{cont}}$ is defined to be a row vector containing the value of $\partial s/\partial b$ at the grid points x_i then, for arbitrary $\delta \mathbf{b}$,

$$(\partial s/\partial \mathbf{b})_{\text{cont}}\mathbf{M} = \partial s/\partial \mathbf{b}. \tag{40}$$

Equivalently, the value of the continuous sensitivity at a grid point $(\partial s/\partial \mathbf{b})_{\text{cont}}$ is given by $(\partial s/\partial \mathbf{b})\mathbf{M}^{-1}$. When dimensional, the dimensions of $\partial s/\partial \mathbf{b}$ are $[s][b]^{-1}$, while the dimensions of $(\partial s/\partial \mathbf{b})_{\text{cont}}$ are $[s][b]^{-1}L^{-\Delta}$, where Δ is the spatial dimension of the problem (1, 2, or 3). The MATLAB function `fun_Helm.m` returns $\partial s/\partial \mathbf{b}$ when the discrete adjoint is requested and $(\partial s/\partial \mathbf{b})_{\text{cont}}$ when the continuous adjoint is requested.

E. Propagating sensitivities through the active iteration method

In the active iteration method, the nonlinear eigenvalue problem (12) is solved as a sequence of linear eigenvalue problems, as described in Sec. III E. At the jth iteration, the operator A in (12) is labeled A_j and depends on s_{j-1} through the time delay term $e^{s_{j-1}\tau}$ and the Robin boundary conditions $k_u(s_{j-1})$ and $k_d(s_{j-1})$. The change in the operator A_j is therefore caused not only by a perturbation to the base state variables at that iteration but also by the shift in the eigenvalue at the previous iteration, acting through $(e^{s_{j-1}\tau})$, k_u, and k_d. To obtain the base state sensitivity exactly, this eigenvalue shift must be propagated through the iterations. The eigenvalue shift at the jth iteration is given by

$$\delta s_j = \int_0^1 \left.\frac{\partial s_j}{\partial b(x)}\right|_{s_{j-1}} \delta b(x) dx \; + \; \left.\frac{\partial s_j}{\partial s_{j-1}}\right|_{b(x)} \delta s_{j-1}, \tag{41}$$

where

$$\left.\frac{\partial s_j}{\partial s_{j-1}}\right|_{b(x)} = \frac{1}{2s_j}\left(\frac{\langle p^\dagger{}_j, (\partial A/\partial s)_{j-1} p_j\rangle}{\langle p^\dagger{}_j, C p_j\rangle}\right) \equiv \xi_j. \tag{42}$$

The eigenvalue shift at the final iteration δs_J is found by applying (41) recursively back to δs_0, which is zero:

$$\delta s_J = \sum_{j=1}^{J} \chi_j \int_0^1 \left.\frac{\partial s_j}{\partial b(x)}\right|_{s_{j-1}} \delta b(x)\, dx \quad \text{with } \chi_j \equiv \begin{cases} 1 & \text{for } j = J \\ \prod_j^{J-1} \xi_j & \text{for } j = 1 \text{ to } J-1. \end{cases} \tag{43}$$

Moving the summation into the integral gives the base state sensitivity of s_J in terms of the base state sensitivities of each iteration s_j, which are listed in Table II:

$$\frac{\partial s_J}{\partial b(x)} = \sum_{j=1}^{J} \chi_j \left.\frac{\partial s_j}{\partial b(x)}\right|_{s_{j-1}}. \tag{44}$$

The quantity χ_j, which can be calculated during the forward iteration, gives the influence of the jth iteration on the final eigenvalue s_J. For a well-converged solution, χ_J is much greater than all the other χ_j and, to a good approximation, δs_J is given by δs_j at the final iteration. This is of practical interest because it reduces the number of direct and adjoint eigenfunctions that need to be stored in order to obtain an accurate base state sensitivity. Another convenient point is that the discrete adjoint codes can be debugged (Sec. V F) by considering just two iterations (i.e., before convergence), which speeds up code development.

F. Debugging the discrete base state sensitivities with a Taylor test

The eigenvalue shift δs for a given base state δb can be calculated via the finite difference: $\delta s = s(b + \delta b) - s(b)$. If the eigenvalue is analytic with respect to the perturbation, this eigenvalue shift can also be expressed as a Taylor expansion

$$\delta s = \frac{\partial s}{\partial b}\delta b + \frac{1}{2}\frac{\partial^2 s}{\partial b^2}(\delta b)^2 + O(\delta b)^3. \tag{45}$$

In the discrete framework, the left and right eigenvectors $\mathbf{p}^\dagger$ and $\mathbf{p}$, respectively, are calculated to machine precision from the same matrix. The first-order sensitivity $\partial s/\partial \mathbf{b}$ in (39) is therefore calculated to machine precision. The difference between δs calculated with a finite-difference method and δs calculated with the adjoint method must therefore increase in proportion to $(\delta b)^2$ and higher orders. If it increases in proportion to δb then there is a bug in the code. This is a stringent and helpful test for debugging. This is implemented in the MATLAB function `fun_TT.m`.

VI. FEEDBACK SENSITIVITY

In this section, the feedback sensitivity is defined (Sec. VI A) and then the theory and numerics are described for the continuous framework (Sec. VI B) and the discrete framework (Sec. VI C), in the `FDS`, `FEW`, `FDW`, and `SBP` formulations. The physical interpretation of the feedback sensitivities is in Sec. VIII B.

A. Linear modeling of passive feedback devices

All feedback devices can be modeled in terms of their feedback from u and/or p into the mass, momentum, and/or energy equations. The feedback can be local in space and time, which would be typical for control via a passive device, or nonlocal, which would be typical for feedback control with a noncolocated sensor and actuator. In this paper, only local feedback will be considered,

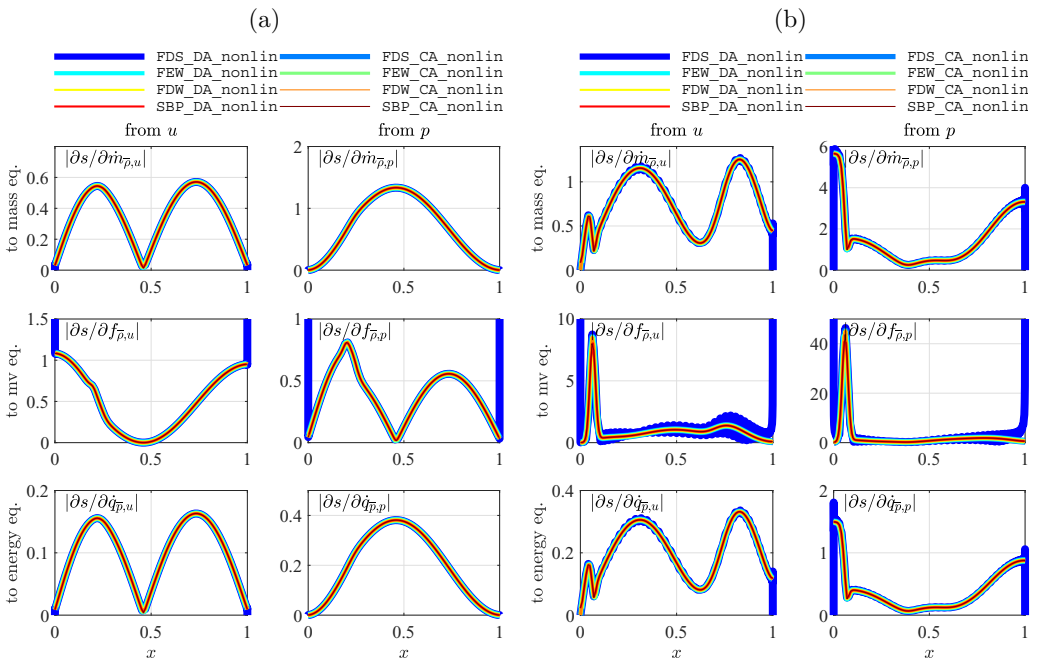

FIG. 5. Absolute values of the feedback sensitivities ($\partial s/\partial \dot{m}_{\overline{\rho},u}$, $\partial s/\partial \dot{m}_{\overline{\rho},p}$, $\partial s/\partial \mathbf{f}_{\overline{\rho},u}$, $\partial s/\partial \mathbf{f}_{\overline{\rho},p}$, $\partial s/\partial \dot{q}_{\overline{\rho},u}$, and $\partial s/\partial \dot{q}_{\overline{\rho},p}$) calculated with the discrete adjoint method (`DA`) and continuous adjoint method (`CA`) for four spatial discretizations (`FDS`, `FEW`, `FDW`, and `SBP`) for the (a) Rijke tube and (b) model rocket engine, for $N = 100$. All lines lie on top of each other except `FDS_DA`, which oscillates. These results were created with `Fig_005.m`.

described by the functions $\delta\dot{m}_{\overline{\rho},u}$, $\delta\dot{m}_{\overline{\rho},p}$, $\delta\mathbf{f}_{\overline{\rho},u}$, $\delta\mathbf{f}_{\overline{\rho},p}$, $\delta\dot{q}_{\overline{\rho},u}$, $\delta\dot{q}_{\overline{\rho},p}$, such that the feedback terms in (10) are local linear functions of u and p:

$$\delta\dot{m}_{\overline{\rho}} = \delta\dot{m}_{\overline{\rho},u}u + \delta\dot{m}_{\overline{\rho},p}p, \tag{46a}$$

$$\delta\mathbf{f}_{\overline{\rho}} = \delta\mathbf{f}_{\overline{\rho},u}u + \delta\mathbf{f}_{\overline{\rho},p}p, \tag{46b}$$

$$\delta\dot{q}_{\overline{\rho}} = \delta\dot{q}_{\overline{\rho},u}u + \delta\dot{q}_{\overline{\rho},p}p. \tag{46c}$$

The change δA to the linear operator A in (12b) is found by substituting (46) into (10).

B. Feedback sensitivity in the continuous framework

The feedback causes a change δA in the operator (12b). The sensitivity of the eigenvalue s to this change is found from the numerator of (33), noting that $\delta G = \delta A$:

$$\begin{aligned}\langle p^\dagger, (\delta A)p\rangle = {} & \langle p^\dagger, s\delta\dot{m}_{\overline{\rho},u}u\rangle + \langle p^\dagger, s\delta\dot{m}_{\overline{\rho},p}p\rangle + \left\langle \frac{dp^\dagger}{dx}, \delta\mathbf{f}_{\overline{\rho},u}u\right\rangle + \left\langle \frac{dp^\dagger}{dx}, \delta\mathbf{f}_{\overline{\rho},p}p\right\rangle \\ & - [p^\dagger\delta\mathbf{f}_{\overline{\rho},u}u + p^\dagger\delta\mathbf{f}_{\overline{\rho},p}p]_0^1 + \langle p^\dagger, s\zeta\delta\dot{q}_{\overline{\rho},u}u\rangle + \langle p^\dagger, s\zeta\delta\dot{q}_{\overline{\rho},p}p\rangle.\end{aligned} \tag{47}$$

In (47), the $\delta\mathbf{f}_{\overline{\rho},u}$ and $\delta\mathbf{f}_{\overline{\rho},p}$ terms have been integrated by parts. Their boundary terms can be calculated but are of little value and are dropped from the subsequent analysis. The eigenvalue shift can be found if the feedback mechanism is known *a priori*. It is more useful, however, to obtain the influence of local feedback at every point in space $\partial s/\partial l(x)$ defined such that $\delta s \equiv \int(\partial s/\partial l)\delta l\, d(x)$, where δl represents the functions $\delta\dot{m}_{\overline{\rho},u}$, $\delta\dot{m}_{\overline{\rho},p}$, $\delta\mathbf{f}_{\overline{\rho},u}$, $\delta\mathbf{f}_{\overline{\rho},p}$, $\delta\dot{q}_{\overline{\rho},u}$, or $\delta\dot{q}_{\overline{\rho},p}$. The feedback sensitivities are listed in Table III and are shown in Fig. 5 (`FDS_CA`, `FEW_CA`, `FDW_CA`,

TABLE III. Feedback sensitivities derived in the continuous framework (47), discretized strong form (48), discretized weak form (49), and discretized SAB SAT form. The inner product α is defined in (33b) and (38). Expressions within parentheses ($\circ$) are functions of x in the continuous framework and row vectors in the discrete frameworks. The symbol $\odot$ denotes element by element multiplication of two row vectors. The final column shows the dimensions of the sensitivities, where Δ is 0 for the discrete frameworks, and the spatial dimension of the problem (1, 2, or 3) for the continuous framework.

Feedback sensitivity	Continuous (`*_CA`)	Discretized strong form (`FDS_DA`)	Discretized weak form (`FEW_DA` and `FDW_DA`)	Discretized SBP SAT strong form (`SBP_DA`)	Dimensions
	$u(x) \equiv -(\overline{v})(dp/dx)/s$	$\mathbf{u} \equiv -(\mathbf{VDp})/s$	$\mathbf{u}_0 \equiv -(\mathbf{V}_{00}\mathbf{D}_{01}\mathbf{p}_1)/s$	$\mathbf{u} \equiv -(\mathbf{V}\mathbf{D}_1\mathbf{p})/s$	U
$(\partial s/\partial \dot{m}_{\overline{p},u})$	$(p^{\dagger *})s(u)/\alpha$	$(\mathbf{p}^{\dagger H}\mathbf{M}s) \odot (\mathbf{u})/\alpha$	$(\mathbf{p}^{\dagger H}_1\mathbf{M}^H_{01}s)_0 \odot (\mathbf{u}_0)/\alpha$	$(\mathbf{p}^{\dagger H}\mathbf{M}s) \odot (\mathbf{u})/\alpha$	$U \times L^{-\Delta}$
$(\partial s/\partial \dot{m}_{\overline{p},p})$	$(p^{\dagger *})s(p)/\alpha$	$(\mathbf{p}^{\dagger H}\mathbf{M}s) \odot (\mathbf{p})/\alpha$	$(\mathbf{p}^{\dagger H}_1\mathbf{M}_{11}s)_1 \odot (\mathbf{p}_1)/\alpha$	$(\mathbf{p}^{\dagger H}\mathbf{M}s) \odot (\mathbf{p})/\alpha$	$P \times L^{-\Delta}$
$(\partial s/\partial \mathbf{f}_{\overline{p},u})$	$(\frac{dp^\dagger}{dx})^*(u)/\alpha$	$-(\mathbf{p}^{\dagger H}\mathbf{MD}) \odot (\mathbf{u})/\alpha$	$(\mathbf{p}^{\dagger H}_1\mathbf{D}^H_{01}\mathbf{M}_{00})_0 \odot (\mathbf{u}_0)/\alpha$	$(\mathbf{p}^{\dagger H}_1\mathbf{D}^H_{01}\mathbf{M}_{00}) \odot (\mathbf{V}_{00}\mathbf{D}_{01}\mathbf{p}/s)/\alpha$	$L^{-\Delta}$
$(\partial s/\partial \mathbf{f}_{\overline{p},p})$	$(\frac{dp^\dagger}{dx})^*(p)/\alpha$	$-(\mathbf{p}^{\dagger H}\mathbf{MD}) \odot (\mathbf{p})/\alpha$	$(\mathbf{p}^{\dagger H}\mathbf{D}^H_{01})_0 \odot (\mathbf{M}_{01}\mathbf{p}_1)_0/\alpha$	$(\mathbf{p}^{\dagger H}\mathbf{D}^H_{01}) \odot (\mathbf{M}_{01}\mathbf{p}_1)/\alpha$	$P \times U^{-1}\ L^{-\Delta}$
$(\partial s/\partial \dot{q}_{\overline{p},u})$	$(p^{\dagger *})s\zeta(u)/\alpha$	$(\mathbf{p}^{\dagger H}\mathbf{M}s\zeta) \odot (\mathbf{u})/\alpha$	$(\mathbf{p}^{\dagger H}_1\mathbf{M}^H_{01}s\zeta)_0 \odot (\mathbf{u}_0)/\alpha$	$(\mathbf{p}^{\dagger H}\mathbf{M}s\zeta) \odot (\mathbf{u})/\alpha$	$U \times L^{-\Delta}$
$(\partial s/\partial \dot{q}_{\overline{p},p})$	$(p^{\dagger *})s\zeta(p)/\alpha$	$(\mathbf{p}^{\dagger H}\mathbf{M}s\zeta) \odot (\mathbf{p})/\alpha$	$(\mathbf{p}^{\dagger H}_1\mathbf{M}_{11}s\zeta)_1 \odot (\mathbf{p}_1)/\alpha$	$(\mathbf{p}^{\dagger H}\mathbf{M}s\zeta) \odot (\mathbf{p})/\alpha$	$P \times L^{-\Delta}$

and SBP_CA). These four lines all lie on top of each other, showing that there are no numerical problems when deriving the feedback sensitivities in the continuous framework.

C. Feedback sensitivity in the discretized strong form equations

For the finite-difference method applied to the strong form Sec. III A, the feedback causes a change $\delta\mathbf{A}$ in the matrix $\mathbf{A}$ [Eq. (13b)] such that

$$\begin{aligned}\delta\mathbf{A} = {} & s\mathbf{M}(\delta\dot{\mathbf{M}}_{\overline{\rho},u})\mathbf{U} + s\mathbf{M}(\delta\dot{\mathbf{M}}_{\overline{\rho},p}) - \mathbf{MD}(\delta\mathbf{F}_{\overline{\rho},u})\mathbf{U} - \mathbf{MD}(\delta\mathbf{F}_{\overline{\rho},p}) \\ & + s\zeta\mathbf{M}(\delta\dot{\mathbf{Q}}_{\overline{\rho},u})\mathbf{U} + s\zeta\mathbf{M}(\delta\dot{\mathbf{Q}}_{\overline{\rho},p}),\end{aligned} \tag{48}$$

where $\mathbf{U} \equiv -\mathbf{VD}/s$ and $\delta\dot{\mathbf{M}}_{\overline{\rho},u}$ is a matrix containing the values of $\delta\dot{m}_{\overline{\rho},u}(x_i)$ along the diagonal. (The other δ matrices are similarly defined.) The eigenvalue shift is then given by (38) with $\delta\mathbf{G} = \delta\mathbf{A}$. The feedback sensitivity in the discrete framework ($\delta s/\delta\mathbf{l}$) is a row vector such that $\delta s = (\partial s/\partial\mathbf{l})\delta\mathbf{l}$. The value of the continuous sensitivity at a grid point point $(\partial s/\partial\mathbf{l})_{\text{cont}}$ is given by $(\partial s/\partial\mathbf{l})\mathbf{M}^{-1}$. These feedback sensitivities are listed in Table III and shown in Fig. 5 (FDS_DA). The problems described in Sec. V C carry through to the feedback sensitivities.

D. Feedback sensitivity in the finite-element framework

In order to implement the feedback terms in the finite-element framework, it is necessary to consider whether each local feedback function $\delta l(x)$ should be a P0 or P1 function. The direct and adjoint eigenfunctions p and $p^\dagger$, respectively, are P1 functions, while u and $dp^\dagger/dx$ are P0 functions. In (47), the inner products containing $\delta\dot{m}_{\overline{\rho},p}$ and $\delta\dot{q}_{\overline{p},p}$ are formed between two P1 functions, so $\delta\dot{m}_{\overline{\rho},p}$ and $\delta\dot{q}_{\overline{p},p}$ are P1 functions. Similarly, the inner product containing $\delta\mathbf{f}_{\overline{\rho},u}$ is formed between two P0 functions, so $\delta\mathbf{f}_{\overline{\rho},u}$ is a P0 function. The remaining three inner products contain both P0 and P1 functions and, because inner products can be formed between P0 and P1 functions using the $\mathbf{M}_{01}$ matrix, one could define $\delta\dot{m}_{\overline{\rho},u}$, $\delta\mathbf{f}_{\overline{\rho},p}$, and $\delta\dot{q}_{\overline{p},u}$ to be either P0 or P1 functions. Their corresponding feedback sensitivities $\partial s/\partial\dot{m}_{\overline{\rho},u}$, $\partial s/\partial\mathbf{f}_{\overline{\rho},p}$, and $\partial s/\partial\dot{q}_{\overline{p},u}$, however, have to be P0 functions. This is because $\mathbf{M}_{01}$ has rank N and its application to a P1 function removes one degree of freedom. Consequently, the feedback sensitivities are element by element multiplication of two row vectors with N degrees of freedom and have to be P0 functions. It is then convenient (although not essential) to define $\delta\dot{m}_{\overline{\rho},u}$, $\delta\mathbf{f}_{\overline{\rho},p}$, and $\delta\dot{q}_{\overline{p},u}$ to be P0 functions as well. With these definitions, the feedback causes a change $\delta\mathbf{A}_{11}$ in the matrix $\mathbf{A}_{11}$ in (15b) such that

$$\begin{aligned}\delta\mathbf{A}_{11} = {} & \mathbf{M}_{10}s(\delta\dot{\mathbf{M}}_{\overline{\rho},u,00})\mathbf{U}_{00} + \mathbf{M}_{11}s(\delta\dot{\mathbf{M}}_{\overline{\rho},p,11}) + \mathbf{D}_{01}^H\mathbf{M}_{00}(\delta\mathbf{F}_{\overline{\rho},u,00})\mathbf{U}_{00} \\ & + \mathbf{D}_{01}^H\mathbf{M}_{00}(\delta\mathbf{F}_{\overline{\rho},p,00})\overline{\mathbf{M}}_{01} + \mathbf{M}_{10}s\zeta(\delta\dot{\mathbf{Q}}_{\overline{p},u,00})\mathbf{U}_{00} + \mathbf{M}_{11}s\zeta(\delta\dot{\mathbf{Q}}_{\overline{p},p,11}),\end{aligned} \tag{49}$$

where $\mathbf{U}_{00} \equiv -\mathbf{V}_{00}\mathbf{D}_{01}/s$. There is a neater way to write the $\delta\mathbf{F}_{\overline{\rho},p,00}$ term in (49). The matrices $\mathbf{M}_{00}$ and $\delta\mathbf{F}_{\overline{\rho},p,00}$ are both diagonal, so their order can be swapped. Then $\mathbf{M}_{00}\overline{\mathbf{M}}_{01}$ can be replaced with $\mathbf{M}_{01}$, as described in Sec. III B. The term then becomes $\mathbf{D}_{01}^H\delta\mathbf{F}_{\overline{\rho},p,00}\mathbf{M}_{01}$. These feedback sensitivities are listed in Table III and shown in Fig. 5 (FEW_DA). The weak form of the finite-difference framework is identical (FDW_DA). These lines lie on top of the other sensitivities, showing that there are no numerical problems when the equations are expressed in the weak form.

E. Feedback sensitivity in the SBP SAT framework

The feedback sensitivities for the finite-difference method applied in the strong SBP SAT form are a combination of the FDS and FEW forms. They are shown in Table III and plotted in Fig. 5 (SBP_DA). There are no numerical problems for this method.

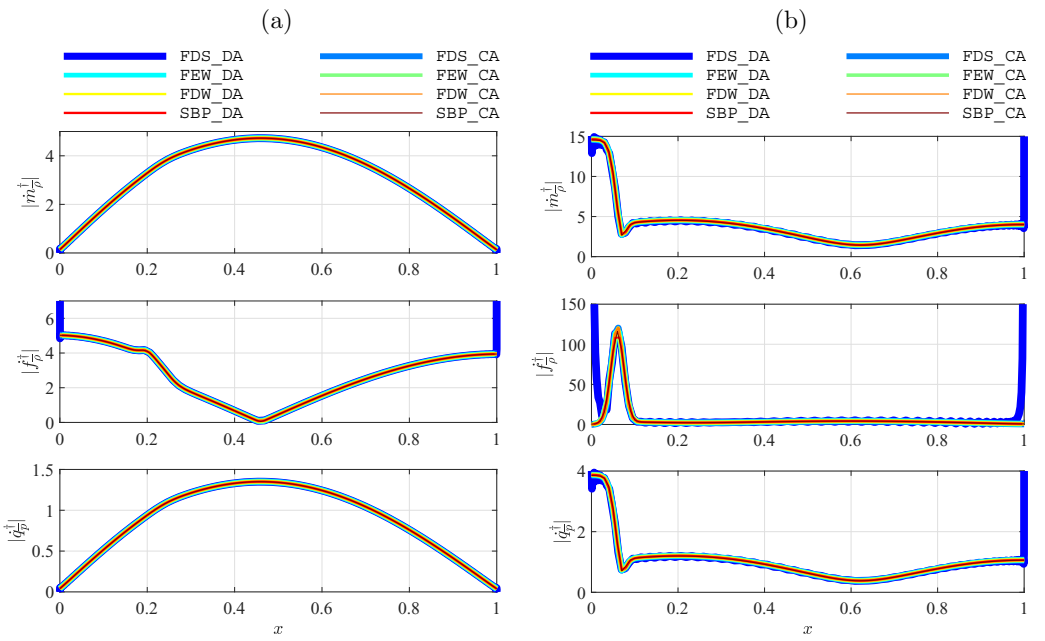

FIG. 6. Absolute values of the receptivity of the eigenvalue to periodic injection of $\dot{m}_{\overline{\rho}}(x)e^{s_f t}$ into the mass equation (2c), $\mathbf{f}_{\overline{\rho}}(x)e^{s_f t}$ into the momentum equation (2d), and $\dot{q}_{\overline{\rho}}(x)e^{s_f t}$ into the energy equation (2e), where s_f is an imaginary number equal to the angular frequency of forcing. From (6), the receptivity of the eigenvalue to mass injection into the mass equation is $\dot{m}^\dagger_{\overline{\rho}}/\overline{\rho}$, momentum injection into the momentum equation is $\mathbf{f}^\dagger_{\overline{\rho}}/\overline{\rho}$, and heat injection into the energy equation is $\dot{q}^\dagger_{\overline{\rho}}/\overline{\rho}$. These are calculated with the discrete adjoint method (`DA`) and continuous adjoint method (`CA`) for four spatial discretizations (`FDS`, `FEW`, `FDW`, and `SBP`) for the (a) Rijke tube and (b) model rocket engine, for $N = 100$. All lines lie on top of each other except `FDS_DA`, which oscillates. This figure was created with `Fig_006.m`.

VII. RECEPTIVITIES

A general approach to receptivity via adjoint equations, which is independent of the solution method, can be found in [37] (Sec. 3.1.1), [38], [10], and [39] (Sec. 2.5). The most relevant result from [39] is for constant amplitude forcing of a stable system. The system in this paper is forced with periodic injection of $\dot{m}_{\overline{\rho}}(x)e^{s_f t}$ into the mass equation (2c), $\mathbf{f}_{\overline{\rho}}(x)e^{s_f t}$ into the momentum equation (2d), and $\dot{q}_{\overline{\rho}}(x)e^{s_f t}$ into the energy equation (2e), where s_f is an imaginary number equal to the angular frequency of forcing. Reference [39] [Eq. (17) therein] shows that the system's linear response has contributions from all eigenfunctions p_k and is at the forcing frequency s_f. For mass injection, the amplitude of the contribution from eigenfunction p_k is proportional to $\langle p_k^\dagger s^*, \dot{m}_{\overline{\rho}}\rangle/(s_f - s_k)$, where s_k is the eigenvalue of p_k. The contribution from eigenfunction p_k is therefore greater (i) the closer s_f is to s_k and (ii) the more the spatial structure of the forcing $\dot{m}_{\overline{\rho}}$ projects onto the function $p_k^\dagger s^*$, which is labeled the receptivity $\dot{m}^\dagger_{\overline{\rho},k}(x)$. [This receptivity is the term to the left of u in the expression for $(\partial s/\partial \dot{m}_{\overline{\rho},u})$ in Table III.] Similarly, the expressions for the receptivities to momentum and heat injection are $\mathbf{f}^\dagger_{\overline{\rho},k} = dp^\dagger_k/dx$ and $\dot{q}^\dagger_{\overline{\rho},k} = {p^\dagger}_k s^* \zeta$, respectively.

Reference [39] [Eq. (18) therein] also shows that, for constant amplitude forcing of a system with one unstable eigenmode k, the system's linear response has frequency or growth rate s_k and spatial structure p_k. As before, the magnitude of the response is greater (i) the closer s_f is to s_k and (ii) the more the spatial structure of the forcing $\dot{m}_{\overline{\rho}}$ projects onto the receptivity $\dot{m}^\dagger_{\overline{\rho},k}(x)$.

The absolute values of the receptivities $|\dot{m}^\dagger_{\overline{\rho}}|$, $|\mathbf{f}^\dagger_{\overline{\rho}}|$, and $|\dot{q}^\dagger_{\overline{\rho}}|$ are shown in Fig. 6 for the dominant mode of the Rijke tube and rocket engine models. These show where the system is most receptive

to open loop forcing. This will be interpreted physically in Sec. VIII A. As expected, there are no numerical problems for the continuous adjoints (`*_CA`) and for the discrete adjoints constructed from the weak form (`FEW_DA` and `FDW_DA`), but there are severe oscillations for the discrete adjoints constructed from the strong form with replacement boundary conditions (`FDS_DA`).

VIII. PHYSICAL INTERPRETATION

A. Receptivities

The most convenient starting point for physical interpretation are the receptivities $|\dot{m}^\dagger_{\overline{\rho}}|$, $|\mathbf{f}^\dagger_{\overline{\rho}}|$, and $|\dot{q}^\dagger_{\overline{p}}|$ in Fig. 6. Using the relations in (6), the sensitivity of the eigenvalue to generic periodic injections of mass into the mass equation $\dot{m}^\dagger$ equals $\dot{m}^\dagger_{\overline{\rho}}/\overline{\rho}$. Similarly, $\mathbf{f}^\dagger = \mathbf{f}^\dagger_{\overline{\rho}}/\overline{\rho}$ and $\dot{q}^\dagger = \dot{q}^\dagger_{\overline{p}}/\overline{p}$. Table III shows that the receptivity of the energy equation $\dot{q}^\dagger$ is proportional to the adjoint pressure eigenfunction $p^\dagger$. In other words, extra heat addition has most influence on the eigenvalue when it is applied to regions in which the adjoint pressure is highest. This can be anticipated from the fact that the adjoint equation (23b) is forced with a term proportional to $\langle \zeta n(e^{-s\tau})h,\, p^\dagger \rangle$. In the self-adjoint case, this becomes equivalent to Rayleigh's criterion [2]. The receptivity of the mass equation $\dot{m}^\dagger$ is proportional to $\overline{v}p^\dagger$. This is similar to $\dot{q}^\dagger$ but includes the fact that mass injection has most influence in regions of lower density.

The receptivity of the momentum equation $\mathbf{f}^\dagger$ is proportional to $\overline{v}dp^\dagger/dx$, which has a clear physical explanation. The heat release term in the adjoint equation (23b) acts in the measurement region (where $dw^*_{\overline{\rho}}/dx \neq 0$), which results in $dp^\dagger/dx$ being largest in this region (Fig. 3). This term therefore reveals that momentum injection has most influence in the measurement region, the more so when the density is smaller ($\overline{v}$ larger) because momentum injection will then cause a larger change in velocity. This describes the unsurprising feature that the eigenvalue is strongly receptive to interference with the velocity in the measurement region.

B. Feedback sensitivities

The feedback sensitivities in Fig. 7 show the real and imaginary components of the absolute values of $|\partial s/\partial l|$ shown in Fig. 5. These are the products of the direct eigenfunctions p and u (Fig. 2) with the receptivities $\dot{m}^\dagger_{\overline{\rho}}$, $\mathbf{f}^\dagger_{\overline{\rho}}$, and $\dot{q}^\dagger_{\overline{p}}$ (Fig. 6). The real component of $\partial s/\partial l$ is the influence of local in-phase feedback on the growth rate (positive denotes destabilizing). The imaginary component is the influence on the frequency.

For the Rijke tube, which is nearly self-adjoint, the real components (thin dark red lines) of $\partial s/\partial \dot{m}_{\overline{\rho},p}$, $\partial s/\partial \mathbf{f}_{\overline{\rho},u}$, and $\partial s/\partial \dot{q}_{\overline{p},p}$ are large and positive. This shows that if mass injection is in phase with pressure, if momentum injection is in phase with velocity, or if energy injection is in phase with pressure (and hence temperature) then the growth rate of oscillations will increase. The most influential positions of such devices are the high-amplitude regions in Fig. 7. This is a restatement of p. 226 of Ref. [3]: "if m' [mass injection] is in phase with p' [acoustic pressure], or F' [momentum injection] with u' [acoustic velocity] or Q' [fluctuating heat release rate] with T' [acoustic temperature] then energy will be continuously fed into the disturbance."

For the rocket engine, which is strongly non-self-adjoint, the real components (thin dark red lines) of $\partial s/\partial \dot{m}_{\overline{\rho},p}$, $\partial s/\partial \mathbf{f}_{\overline{\rho},u}$, and $\partial s/\partial \dot{q}_{\overline{p},p}$ are large, but not always positive. Upstream of the measurement region ($X_w = 0.06$), the growth rate of oscillations will decrease if mass injection is in phase with pressure, if momentum injection is in phase with velocity, or if heat injection is in phase with temperature. This differs from Chu's statement [3] because, as shown in Sec. VII, the receptivities of the mass, momentum, and energy equations need to be formed with the adjoint pressure $p^\dagger$ rather than the direct pressure p. For the rocket, $p^\dagger$ differs considerably from p. For comparison, the feedback sensitivities when the receptivities are formed with the direct pressure p are also shown in Fig. 7 (thick light blue and red lines). The real components (thick light red lines) of these (incorrect) versions of $\partial s/\partial \dot{m}_{\overline{\rho},p}$, $\partial s/\partial \mathbf{f}_{\overline{\rho},u}$, and $\partial s/\partial \dot{q}_{\overline{p},p}$ are always positive, as

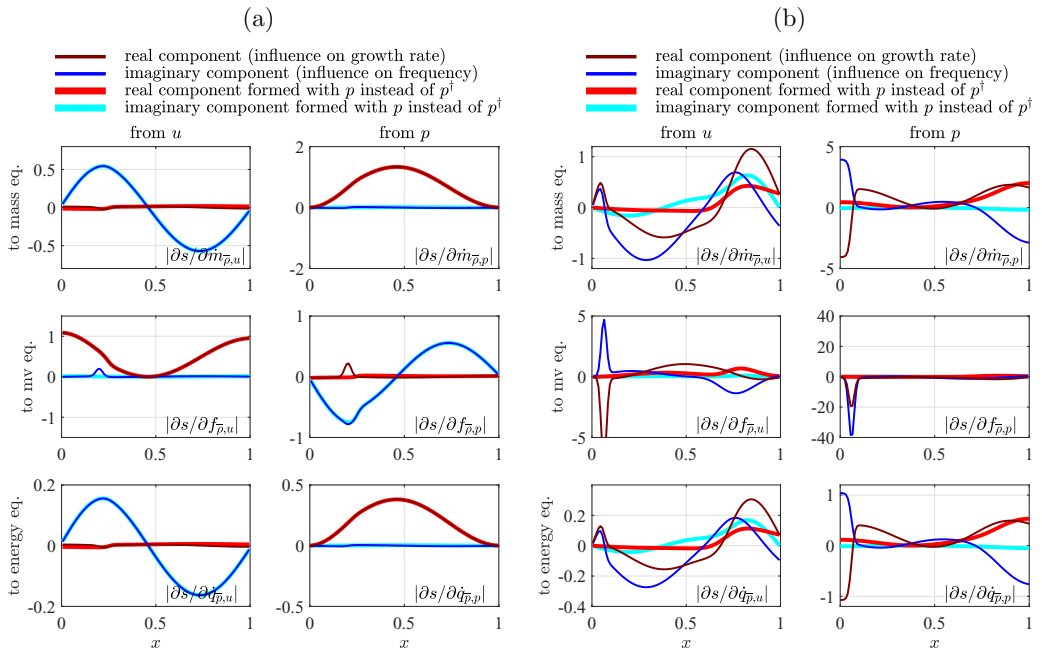

FIG. 7. Real and imaginary components of the feedback sensitivities in Fig. 5, calculated with discrete adjoint (DA) of the finite-element method (FEW) for the (a) Rijke tube and (b) model rocket engine, for $N = 100$. The wider lines show the same sensitivities calculated when the adjoint pressure $p^\dagger$ is replaced by the direction pressure p, i.e., as if the system were self-adjoint. There is little difference for the Rijke tube, which is weakly non-self-adjoint, but a large difference for the rocket engine, which is strongly non-self-adjoint. This figure was created with `Fig_007.m`.

expected from Chu's statement. Further, for the Rijke tube, they are almost identical to the correct feedback sensitivities because the Rijke tube is nearly self-adjoint. This conclusion carries over into the Rayleigh criterion, which states that the acoustic energy grows over a cycle if $\oint pq\,dt$ exceeds the damping. In a linear stability analysis, p in the Rayleigh criterion should be replaced with the receptivity of the energy equation $\dot{q}^\dagger$, which is proportional to the adjoint pressure $p^\dagger$ rather than the direct pressure p. This makes a significant difference in strongly non-self adjoint systems.

C. Base state sensitivities

The base state sensitivities in Fig. 8 show the real and imaginary components of the absolute values in Fig. 4. The sensitivity of the eigenvalue to changes in $h(x)$ has the shape of the adjoint pressure eigenfunction $p^\dagger$ and amplitude $\zeta n e^{-s\tau} \int w_{\overline{p}}(dp/dx)dx$. In physical terms, the shape follows that of the receptivity of the energy equation and the amplitude is large if the measurement function $w_{\overline{p}}$ is large in regions in which the velocity is large. If τ varies in space, then this sensitivity oscillates in space. The sensitivity to changes in $\tau(x)$ is significant only in the heat release region $h(x) > 0$. The sensitivity to changes in the measurement region $w_{\overline{p}}$ has the shape of the direct velocity and amplitude $\langle p^\dagger, \zeta n e^{-s\tau} h\rangle$. In physical terms it is proportional to the local velocity in the measurement region and to the Rayleigh integral formed with the adjoint pressure. The base state sensitivities formed by replacing the adjoint pressure $p^\dagger$ with the direct pressure p are shown for comparison. As expected, there is little discrepancy for the Rijke tube, which is nearly self-adjoint, but significant discrepancy for the rocket engine, which is strongly non-self adjoint.

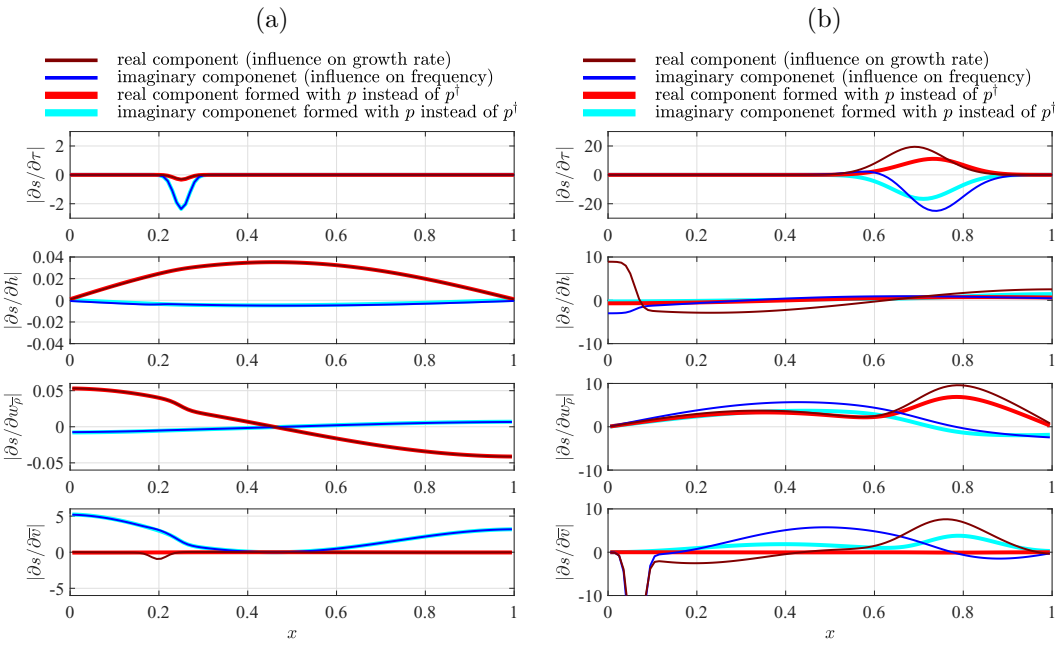

FIG. 8. Real and imaginary components of the base state sensitivities in Fig. 4, calculated with discrete adjoint (`DA`) of the finite-element method (`FEW`) for the (a) Rijke tube and (b) model rocket engine, for $N = 100$. As in Fig. 7, the wider lines show the base state sensitivities formed when the adjoint pressure $p^\dagger$ is replaced by the direction pressure p, i.e., if the system is assumed to be self-adjoint. This figure was created with `Fig_008.m`.

IX. APPLICATIONS OF THE BASE STATE SENSITIVITIES

The base state sensitivities (Fig. 8) show, at a glance, how the growth rate and frequency of the thermoacoustic mode are affected by changes to the base state parameters at each point in space and by changes to the boundary conditions. This is useful for physical understanding of how the thermoacoustic mechanism acts in a given system and can inform strategies to reduce thermoacoustic instability. Further, these base state sensitivities can cheaply be converted into sensitivities to the design parameters. This allows a design procedure to be automated such that every unstable thermoacoustic mode can be stabilized by making small changes to the design parameters. For a network model with longitudinal waves only, this procedure is demonstrated for a laboratory burner in [15]. In this case, which was chosen for its difficulty, the seven initially unstable modes are all stabilized by making small geometry changes. For a network model with longitudinal and azimuthal waves only, this procedure is demonstrated for axisymmetric changes to an annular gas turbine combustion chamber in [16]. In this case, which was chosen for its realism, the two initially unstable modes are both stabilized by changing areas and lengths by no more than 6%. Here the procedure is demonstrated for 1D Helmholtz solvers.

A. Design parameter sensitivities

Table II contains the base state sensitivities to the internal parameters $\overline{v}(x)$, n, $\tau(x)$, $h(x)$, $w_{\overline{p}}(x)$. In the corresponding MATLAB codes, these internal parameters are functions of external (design) parameters X_w, L_w, X_h, L_h, τ, R_u, R_d, which are set in `fun_param_dim.m`. The sensitivities of the eigenvalue with respect to the external parameters are found using the chain rule. For example, the sensitivity with respect to the heat release location X_h, keeping all other design parameters constant,

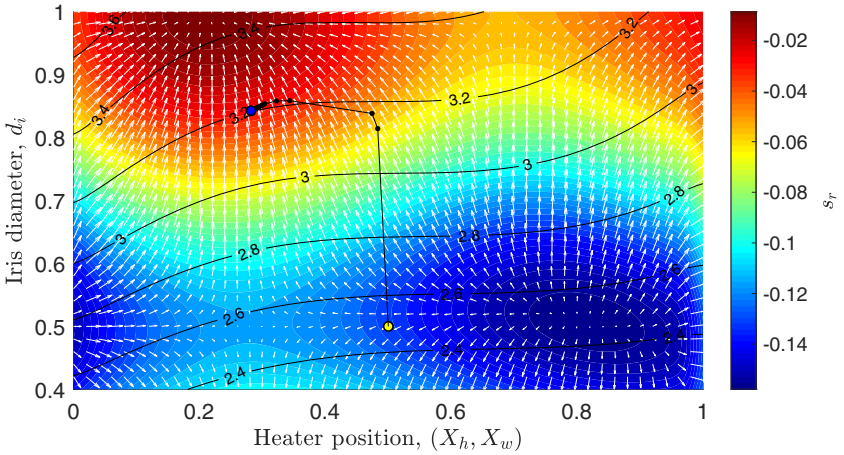

FIG. 9. Growth rates (color contours) and nondimensional frequencies (black line contours) for the Rijke tube with a variable-diameter iris placed at the downstream boundary and a variable heater position (X_h, X_w). A quasi-Newton algorithm uses adjoint-based gradient information (white arrows) to converge to the point with maximum growth rate at a user-defined frequency, in this case 3.2. This figure was created with `Fig_009.m`.

is

$$\left.\frac{\partial s}{\partial X_h}\right|_{X_w \cdots R_d} = \int_0^1 \left(\frac{\partial s}{\partial h}\frac{\partial h}{\partial X_h} + \frac{\partial s}{\partial \overline{v}}\frac{\partial \overline{v}}{\partial X_h} + \frac{\partial s}{\partial w_{\overline{\rho}}}\frac{\partial w_{\overline{\rho}}}{\partial X_h} \right) dx \tag{50}$$

in the continuous form and

$$\left.\frac{\partial s}{\partial X_h}\right|_{X_w \cdots R_d} = \frac{\partial s}{\partial \mathbf{h}}\frac{\partial \mathbf{h}}{\partial X_h} + \frac{\partial s}{\partial \overline{\mathbf{v}}}\frac{\partial \overline{\mathbf{v}}}{\partial X_h} + \frac{\partial s}{\partial \mathbf{w}_{\overline{\rho}}}\frac{\partial \mathbf{w}_{\overline{\rho}}}{\partial X_h} \tag{51}$$

in the discrete form. The partial derivatives on the right-hand side are returned by `fun_h.m`, `fun_rh.m`, and `fun_wr.m`. Some of the external parameters, such as the heat release position, are known accurately. Others, such as the heat release time delay and reflection coefficients, are not. By calculating these sensitivities, the user can discover which parameters have most influence on the experimental measurements and therefore which need to be measured accurately. These sensitivities are also useful for rapid uncertainty quantification, as shown for a thermoacoustic network model in [40].

B. Gradient-based optimization with adjoints

In thermoacoustics, gradient-based shape optimization with adjoints has been applied via a network model in [15,16]. In the current paper, realistic burner geometries cannot be considered because the adjoint Helmholtz solver is one dimensional. Nevertheless, gradient-based optimization of a Rijke tube with adjoints can be demonstrated. Figure 9 shows the nondimensional growth rates (color contours) and nondimensional frequencies (black line contours) for the Rijke tube with a variable-diameter iris placed at the downstream boundary and a variable heater position. The reflection coefficient R_d is assumed to be a function of the iris diameter d_i such that $R_d = 0.97\cos(\pi d_i) + 0.80i\sin(\pi d_i)$. Here the measurement point X_w is the same as the heat release point X_h. The gradient of s_r with respect to X_h and d_i, as calculated with the base state sensitivity, is shown by the white arrows. This confirms that the arrows point in the correct direction. An optimization algorithm using a BFGS quasi-Newton algorithm with an Armijo line search and a penalty function is used to converge from a starting point (light dot) to the point with the maximum

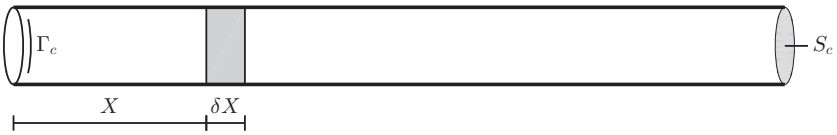

FIG. 10. Diagram of a Rijke tube with perimeter Γ_c and cross-sectional area S_c containing a passive feedback device at position X with width δX.

growth rate at a target frequency (dark dot). In this case the target frequency is 3.2. The gradient information is used in the quasi-Newton method to estimate the inverse Hessian, which greatly speeds up the rate of convergence compared with other algorithms.

X. APPLICATIONS OF THE FEEDBACK SENSITIVITIES

The design parameter sensitivities, which are derived from the base state sensitivities, show the influence of small changes to a given design. However, they do not show the influence of a qualitative change to the design, such as adding a new component. This influence can be calculated at negligible extra cost by multiplying the feedback sensitivities by a number, as described in this section. This is useful because many industrial gas turbines are stabilized by retrofitting passive feedback devices such as Helmholtz resonators. The techniques in this section show the best locations for such devices and, within the bounds of a linear analysis, can calculate their influence on the eigenvalues. The feedback sensitivities can also be used to estimate the influence of features such as the viscous and thermal boundary layers that exist in reality but are not included in this model.

A. Calculating the influence of an adiabatic mesh

In the experiments of [33] on the electrically heated Rijke tube being modeled in this paper, the shift in growth rate is measured when a mesh of width δX is introduced at position X_m (Fig. 10). The drag force of the mesh on the flow can be considered as local instantaneous feedback from the acoustic velocity into the acoustic momentum equation. Its influence on the growth rate and frequency can be estimated with the feedback sensitivity $\partial s/\partial \mathbf{f}_{\overline{\rho},u}$. The pressure drop across the mesh is assumed to be $\Delta p = -K\overline{\rho}(\overline{u}+\tilde{u})^2/2$, where $\overline{u}$ is the mean velocity, $\tilde{u}$ is the fluctuating velocity, and K is a quasisteady pressure drop coefficient. In the experiments of [33], the mean speed $\overline{u}$ is estimated as 0.1 $\mathrm{m\,s^{-1}}$ and K is estimated as 20, based on the ratio of free area to total area of the wire mesh [41]. The total fluctuating force is therefore $-S_c K\overline{\rho u}\tilde{u}$, where S_c is the cross-sectional area of the tube. This acts over a volume $S_c\delta X$ so the fluctuating force per unit volume is $\delta\tilde{\mathbf{f}} = \overline{\rho u}\tilde{u}K/\delta X$. Applying the definitions (6) and (46b) and moving to the frequency domain in one spatial dimension gives $\delta\mathbf{f}_{\overline{\rho},u} = \overline{u}K/\delta X$. Substituting into (37), assuming uniformity over δX_m, and expressing in dimensional form (Table III with $\Delta = 1$) gives

$$\delta s^\star = \int_{X_m}^{X_m+\delta X} \frac{1}{L_{\mathrm{ref}}}\left(\frac{\partial s}{\partial \mathbf{f}_{\overline{\rho},u}}\right)^\star \delta\mathbf{f}_{\overline{\rho},u}\,dx = \frac{\overline{u}K}{L_{\mathrm{ref}}}\left(\frac{\partial s}{\partial \mathbf{f}_{\overline{\rho},u}}(X_m)\right)^\star = -2.0\left(\frac{\partial s}{\partial \mathbf{f}_{\overline{\rho},u}}(X_m)\right)^\star. \tag{52}$$

The growth rate shift predicted from (52) compares favorably with that measured experimentally in Fig. 11, as a function of the position of the mesh X_m. The maximum growth rate shift of -2 $\mathrm{rad\,s^{-1}}$ is a useful benchmark against which to compare the growth rate shifts in the following sections.

B. Calculating the influence of a hot mesh

In the experiments of [42], the shift in growth rate is measured when a hot mesh of width δX is introduced at position X_m. The heat transfer from the mesh to the flow can be considered as local feedback from the acoustic velocity into the acoustic energy equation with a small time delay. Its influence on the growth rate and frequency can be estimated with the feedback sensitivity $\partial s/\partial \dot{q}_{\overline{p},u}$.

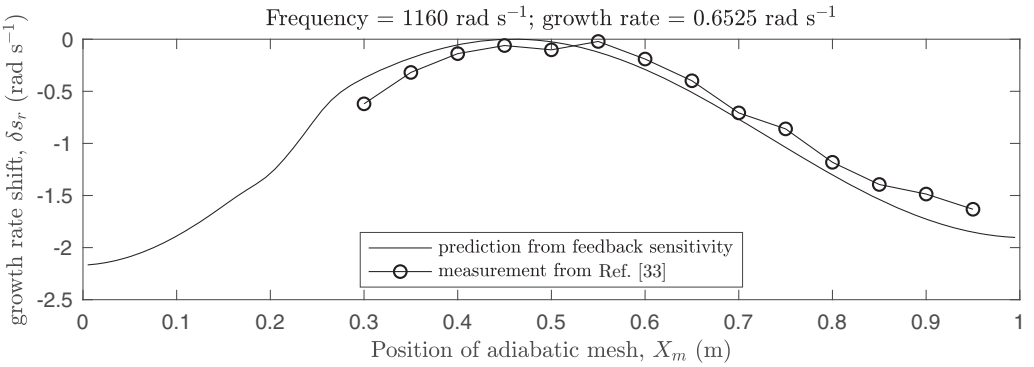

FIG. 11. Growth rate shift caused by drag from an adiabatic mesh placed at position X_m.

The heat transfer model is assumed to be the same as that of the main hot mesh, i.e., an n-τ model with the same time delay τ, FTF, and mean flow speed $\overline{u}$ but a different power $\dot{Q}_m$. This gives $\eta_m = \dot{Q}_m|\mathrm{FTF}|/\overline{u}$. The measurement location and heat release location are both set to X_m. The heat release per unit volume at X_m is therefore $\delta\tilde{\dot{q}} = \eta_m \tilde{u} e^{s\tau}/S_c \delta X$. The dimensional shift in the eigenvalue is

$$\delta s = \frac{U_{\mathrm{ref}}}{L_{\mathrm{ref}}} \frac{\eta_m}{\overline{p} S_c} e^{s\tau} \left(\frac{\partial s}{\partial \dot{q}_{\overline{p},u}}(X_m) \right)^\star = (-9.2 - 54i) \left(\frac{\partial s}{\partial \dot{q}_{\overline{p},u}}(X_m) \right)^\star . \tag{53}$$

The eigenvalue shift per unit power of the secondary heater is plotted in Fig. 12. This shows that the largest growth rate shift due to the heat release from the secondary hot mesh exceeds that due to the drag from the secondary hot mesh when the secondary heater power exceeds around $2.0/0.05 = 40$ W. This is a useful rule of thumb when designing experiments. The comparison with the experimental results of [42] shows an offset. This is due to a change in the base state caused by the secondary heater, which is not considered in the current model but which has been included in Ref. [43]. Finally, the results in this section can be checked by making the secondary hot mesh identical to the primary hot mesh $\eta_m = \eta$, removing damping by setting $R_u = R_d = -1$, and checking that the growth rate shift due to the secondary hot mesh is equal to the growth rate due to the primary hot mesh when they are both in the same position. This can be checked by running `Sup_003.m` [34].

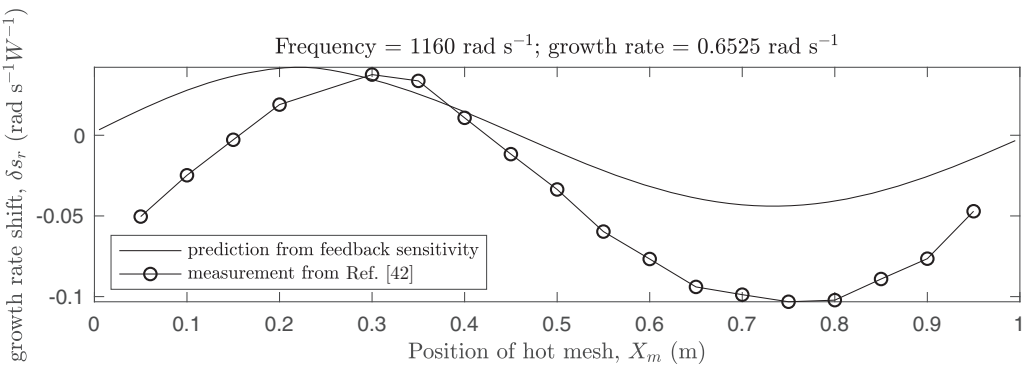

FIG. 12. Growth rate shift caused by drag from a secondary hot mesh placed at position X_m. The offset is caused by a change to the base state induced by the secondary hot mesh [43].

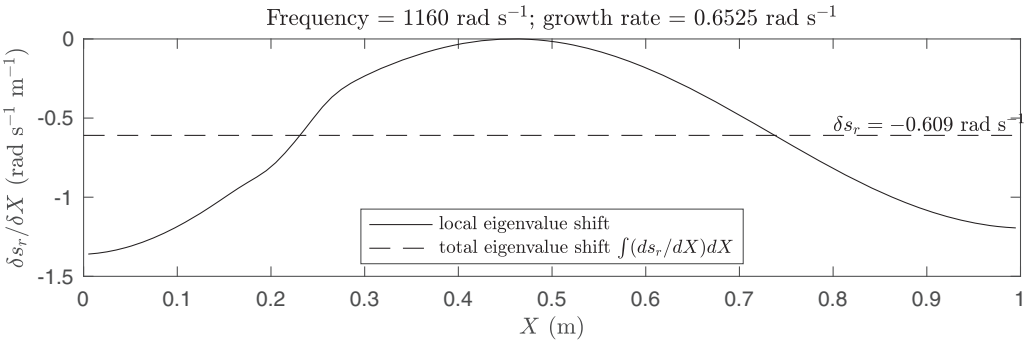

FIG. 13. Growth rate shift caused by the viscous acoustic boundary layer, estimated with the feedback sensitivity.

C. Calculating the influence of the viscous boundary layer

The viscous acoustic boundary layer has not been included in the model. Its influence on the eigenvalue can be estimated with the feedback sensitivity as an *a posteriori* check that its omission from the model is justified. For a simple analysis, the fluctuating wall shear stress τ_m can be approximated as $-\overline{\rho}\nu\tilde{u}/\delta_{bl}$, where ν is the kinematic viscosity, $\tilde{u}$ is the free stream perturbation velocity, and $\delta_{bl}(x)$ is the local acoustic boundary layer thickness. The acoustic boundary layer thickness can be estimated from Stokes' solution for oscillatory flow at angular frequency s_i above a stationary boundary: $\delta_{bl} = 2\pi(2\nu/s_i)^{1/2}$. For an element of tube with length δX and perimeter Γ_c, the total fluctuating force is therefore $-\Gamma_c\delta X\overline{\rho}\nu\tilde{u}/\delta_{bl}$. Following the same analysis as that in Sec. X A gives the local eigenvalue shift per unit length of the boundary layer:

$$\frac{\delta s}{\delta X} = -\frac{1}{L_{\text{ref}}}\frac{\Gamma}{S_c}\frac{\nu}{\delta_{bl}}\left(\frac{\partial s}{\partial \mathbf{f}_{\overline{\rho},u}}(X)\right)^{\star} = 1.26\left(\frac{\partial s}{\partial \mathbf{f}_{\overline{\rho},u}}(X)\right)^{\star}. \tag{54}$$

The results are shown in Fig. 13, showing that the total decay rate due to the viscous boundary layer, integrated along the length of the chamber, is approximately -0.61 rad s^{-1}. The local decay rate is largest at the ends of the tube, where the acoustic speed is largest. For comparison, the decay rate due to acoustic radiation from the tube is around -10 rad s^{-1}. (This can be calculated by setting $\dot{Q}_h = 0$ in `fun_param_dim.m`.) The decay due to the viscous boundary layer is therefore around 6% of that due to acoustic radiation from the open ends of the tube, which is sufficiently small to be neglected from the current analysis.

D. Calculating the influence of the thermal boundary layer

Similarly, the influence of the thermal boundary layer can be calculated with the feedback sensitivity. The gas temperature is $\overline{T} + \tilde{T}$. The wall is assumed to be in thermal equilibrium with the local mean flow at $\overline{T}$. The heat transfer into the gas from an element of tube with length δX and perimeter Γ_c is $\delta\tilde{q} = -(\Gamma_c\delta X)(\lambda/\delta_{bl})\tilde{T}$, where δ_{bl} is the local thermal boundary layer thickness and $\lambda = \overline{\rho}\nu c_p/\text{Pr}$. The acoustic thermal boundary layer thickness is taken to be the same as the acoustic momentum boundary layer thickness. The Prandtl number is set to $\text{Pr} = 0.7$ and, by construction, $P_{\text{ref}} = \overline{p}$. Sound waves are isentropic so $\tilde{T}/\overline{T} = (\tilde{p}/\overline{p})(\gamma - 1)/\gamma$. Using the ideal gas law $\overline{p} = \overline{\rho} r_g \overline{T}$, the above expressions can be combined to obtain $\delta\tilde{q} = -\Gamma_c\delta X\nu\tilde{p}/\text{Pr}\delta_{bl}$. The thermal boundary layer is therefore modeled as a feedback term from the pressure into the energy equation. Following analysis similar to that in Sec. X C gives the local eigenvalue shift per unit length of the boundary layer:

$$\frac{\delta s}{\delta X} = -\frac{P_{\text{ref}}}{L_{\text{ref}}}\frac{\Gamma_c}{S_c}\frac{\nu}{\delta_{bl}}\frac{1}{\text{Pr}}\frac{1}{\overline{p}}\left(\frac{\partial s}{\partial \dot{q}_{\overline{p},p}}(X)\right)^{\star} = 1.79\left(\frac{\partial s}{\partial \dot{q}_{\overline{p},p}}(X)\right)^{\star}. \tag{55}$$

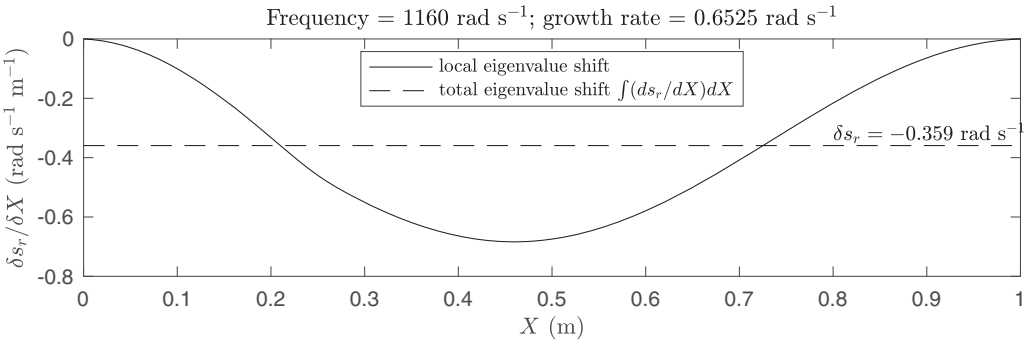

FIG. 14. Growth rate shift caused by the thermal acoustic boundary layer, estimated with the feedback sensitivity.

This produces the results in Fig. 14. It can be seen that the thermal boundary layer is slightly less influential than the viscous boundary layer and that it has most influence at the center of the tube, where the pressure fluctuations are largest.

E. Optimal positioning and sizing of a Helmholtz resonator

Helmholtz resonators are often used in gas turbines to damp particular frequencies. They consist of a cavity, which is connected by a neck to the system that will be damped. Viscous dissipation and vortex shedding at both ends of the neck extract mechanical energy from the oscillation. The closer the oscillation is to the resonant frequency of the resonator, the larger the oscillation in the neck is and the more acoustic oscillations are damped. In this paper, a Helmholtz resonator with mean flow through the neck is considered because this has a linear relationship between the velocity of air flowing into the resonator $\tilde{u}_n$ and the pressure just outside the neck $\tilde{p}_n$ (see [44], Sec. 5.2.5),

$$\tilde{u}_n = \frac{\tilde{p}_n}{Z\overline{\rho}c_0}, \tag{56}$$

where

$$Z = \frac{1-(\omega/\omega_R)^2 + i\,\mathrm{Ma}_n\omega_n\omega/\omega_R^2}{\mathrm{Ma}_n + i\omega_n\omega/\omega_R^2},$$

where Ma_n is the Mach number of the mean flow in the neck, ω is the angular frequency of oscillations, ω_R is the resonant angular frequency of the resonator, and $\omega_n = c_0/(L_n + \delta_n)$, where L_n is the neck length and δ_n is the end correction. The dependence of ω_R and ω_n on the geometrical parameters of the resonator can be found in [44] and in `Fig_015.m`. The resonator is driven by the pressure oscillations and forces the mass equation. (In this paper, its influence on the momentum and entropy equations will be neglected for simplicity.)

For a resonator with neck cross-sectional area S_n the fluctuating mass injection is $-\overline{\rho}S_n\tilde{u}_n$. This acts at position X_n over a region δX. Here ω_R is taken to be 1020 rad s^{-1} in a chamber for which $\omega = s_i = 1160$ rad s^{-1}. Following an analysis similar to that in Sec. X A, the dimensional eigenvalue shift is

$$\delta s = -\frac{P_{\mathrm{ref}}}{L_{\mathrm{ref}}}\frac{S_n}{S_c}\frac{1}{\overline{\rho}c_0}\frac{1}{Z}\left(\frac{\partial s}{\partial \dot{m}_{\overline{\rho},p}}(X_n)\right)^\star = (-46.3+142i)\left(\frac{\partial s}{\partial \dot{m}_{\overline{\rho},p}}(X_n)\right)^\star. \tag{57}$$

This is shown in Fig. 15, which was calculated with `Fig_015.m`. As expected, the growth rate shift depends strongly on ω/ω_R, as can be seen by changing the Helmholtz resonator geometric parameters in `Fig_015.m`. The main point to note, however, is that the Helmholtz resonator is orders

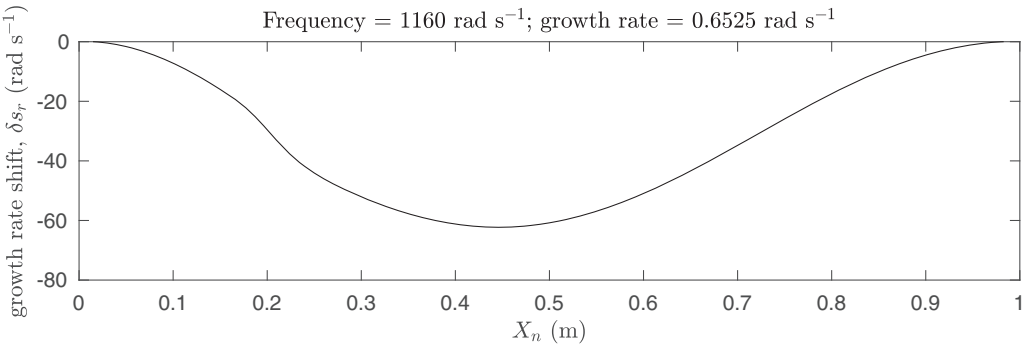

FIG. 15. Growth rate shift of an oscillation at $\omega = 1160$ rad s^{-1} due to a Helmholtz resonator with natural frequency $\omega_R = 1020$ rad s^{-1}, as a function of the resonator position X_n.

of magnitude more influential than a cold mesh, a hot mesh, or the viscous and thermal boundary layers, as expected.

The optimal position of the Helmholtz resonator, which is the point at which the real component of δs reaches a minimum, depends on the complex impedance of the Helmholtz resonator because $\partial s/\partial \dot{m}_{\overline{\rho},p}$ is complex. In turn this depends on Ma_n, ω_n, and ω_R, which depend in turn on the resonator's geometry. Further, the resonator's geometry may be constrained by the geometry of the engine. Although this leads to a technically difficult constrained optimization problem, optimization is greatly helped by the fact that the variation of s with respect to every geometric parameter can be calculated with the chain rule. This can be used in a gradient-based optimization algorithm.

XI. CONCLUSION

This paper showed how to implement adjoint thermoacoustic Helmholtz solvers and how to use the results for physical understanding, gradient-based optimization, and rapid estimation of the influence of retrofitted devices and phenomena omitted from a model. The paper compared four discretization techniques (finite difference of the strong form with replacement boundary conditions, finite element of the weak form, finite difference of the weak form, and summation by parts finite difference of the strong form with a simultaneous approximation term for the boundary conditions), two iteration techniques (a Newton method and an iterative linear method), and two adjoint techniques (discrete adjoint and continuous adjoint), making a total of 16 combinations. MATLAB codes were provided to implement all 16 combinations and to create every figure in the paper.

The direct and adjoint eigenmodes were combined in different ways to reveal (i) the sensitivity of the eigenvalue to changes in the internal and external model parameters (the base state sensitivity), (ii) the sensitivity of the eigenvalue to qualitative changes to the model that introduce local feedback (the feedback sensitivity), and (iii) the receptivity of the system to open loop forcing of the mass, momentum, and energy equations. The paper showed how the receptivities and base state sensitivities aid physical understanding of the thermoacoustic mechanism and how they can automate a design process to stabilize the system. The paper also showed how the feedback sensitivity can be used to test model assumptions *a posteriori* and to identify the optimal location of retrofitted damping devices.

Regarding numerical implications, all 16 combinations gave the same result when Dirichlet boundary conditions on pressure were imposed. When Neumann or Robin boundary conditions were imposed by replacing rows in the matrix operators, the discrete adjoint of the finite-difference discretization of the strong form equations (`FDS_DA`) contained oscillations that propagated into some of the base state and feedback sensitivities. The reasons for this were explained in Secs. IV B and V C. The replacement method used for the `FDS_DA` method should therefore be avoided. All the other methods work well for all boundary conditions, so the choice of method will depend on

practical considerations, such as the methods used in any preexisting code. If there is no preexisting code then the easiest and safest approach is to implement the direct equations in the weak form and to use the discrete adjoint (`FEW_DA` and `FDW_DA`). This allows all discretizations to be used, with boundary conditions that are straightforward to implement. The adjoint eigenvector is then simply the left eigenvector of the corresponding generalized matrix eigenvalue problem. If the direct equations in the strong form must be used and if the discrete adjoint is desired, then the discretization must obey a summation by parts formula, with boundary conditions imposed with a simultaneous approximation term (`SBP_DA`). Summation by parts simultaneous approximation term schemes have been devised for high-order schemes on uniform grids [31,32] and on nonuniform grids [45,46], so this is feasible, although technically more challenging than using the weak form. When using the discrete adjoint, one must not forget the relationship between the discrete and continuous sensitivities (Sec. V D). The continuous adjoint can be used with any discretization, but one must pay close attention to the adjoint boundary conditions (Sec. V A).

Expressions for the base state sensitivities are in Table II and the feedback sensitivities are in Table III. These are valid in one, two, or three dimensions. Both iteration techniques work well, but the iterative linear method (active iteration) is more robust. If active iteration is used then the sensitivities need to be propagated through the steps as detailed in Sec. V E. A neat advantage of the active iteration method is that the adjoint code can be debugged using Taylor tests (Sec. V F) with a single iteration, i.e., before the direct code has converged.

Regarding physical implications, the receptivities (Sec. VII) give physical insight into the thermoacoustic mechanism in a given system. Comparison of the direct equation (12b) with the continuous adjoint equation (23b) showed that the adjoint pressure eigenfunction deviates increasingly from the pressure eigenfunction as the interaction index n increases and as the distance between the measurement region and the heat release region increases. This was demonstrated by comparing the Rijke tube with a simple model of a rocket engine. For this reason, the quote from Chu [3] in Sec. I, which was derived by considering perturbations to a self-adjoint system, is not correct for non-self-adjoint systems. Instead it is more accurate to examine the feedback sensitivities formed, correctly, with the adjoint pressure rather than the direct pressure. For the same reason, the generalized Rayleigh criterion should be formed with the adjoint pressure. The Rayleigh criterion formed with the direct pressure is the special case for self-adjoint systems. The feedback sensitivities show that the viscous and thermal boundary layers can safely be omitted from the model under the conditions examined in this paper. They also show why a Helmholtz resonator damps oscillations much more than an adiabatic mesh or a hot mesh.

In summary, this paper laid out the theory, numerics, and applications of adjoint thermoacoustic Helmholtz solvers. The desirable next step is to apply these techniques to 2D and 3D Helmholtz solvers and then to apply shape optimization in order to stabilize complex geometries such as gas turbines. Engineering applications will impose further constraints, but these can be incorporated into the model or into the optimization procedure. This process has the potential to speed up the design process of gas turbines and rocket engines, whether for optimal retrofitting of damping devices or for tweaking a current device to eliminate thermoacoustic oscillations. Given the extreme sensitivity often found in thermoacoustic systems, and hence the strong influence of small changes, adjoint Helmholtz solvers should be a valuable tool for gas turbine and rocket engine designers in the future.

ACKNOWLEDGMENTS

The author is grateful to the Center for Turbulence Research Summer Program (Stanford University). The author wishes to thank Luca Magri for useful discussions during the course of the project and the two reviewers for their suggested improvements to the paper.

APPENDIX

This Appendix provides MATLAB scripts and functions [34].

`Run_Helm.m`

Read in the dimensional parameters with `fun_param_dim.m`.
Calculate the reference scales and nondimensional parameters with `fun_nondim.m`.
Set the numerical scheme, starting s, and number of iterations J.
Call `fun_Helm.m`.
Plot the requested output.
Perform a Taylor test if requested.

Input arguments

name	values/type	description/contents
`discretization`	`FDS`, `FEW`, `FDW`, or `SBP`	as for `fun_Helm.m`
`type_of_adjoint`	`DA` or `CA`	as for `fun_Helm.m`
`lin_or_nonlin`	`nonlin` or `linear`	as for `fun_Helm.m`
`plot_type` (optional)	`emode`, `bs_sens`, `fb_sens`, `rec`	Output to be plotted: eigenmode, base state sensitivities, feedback sensitivities, or receptivities
`TT_int` (optional)	cell array	as for `fun_Helm.m`
`TT_ext` (optionsl)	cell array	as for `fun_Helm.m`

Example calls from the run line

```
>> Run_Helm('FDS','CA','nonlin')
>> Run_Helm('FEW','DA','nonlin','emode')
>> Run_Helm('FDW','CA','linear','bs_sens')
>> Run_Helm('SBP','DA','linear','fb_sens',{'t'},{})
>> Run_Helm('FDW','DA','linear','rec',{'all'},{'all'})
```

`fun_Helm.m`

Read in the grid-point positions and discretization matrices (`FE`, `FE`, or `SBP`).
Construct matrices **A** and **C** using the relevant discretization (`FDS`, `FEW`, `FDW`, or `SBP`)
and boundary conditions.
Iterate to find the left eigenvector, eigenvalue, and right eigenvector.
Read in the matrices that transform the eigenvectors into receptivities.
Wrap the outputs into the `emode` structure and return if no sensitivities are requested.
Calculate and return the internal sensitivities `ds_int`.
Calculate and return the external sensitivities `ds_ext`.
Perform a Taylor test if requested.

Input arguments

name	values/type	description/contents
`discretization`	`FDS`, `FEW`, `FDW`, or `SBP`	Type of spatial discretization
`type_of_adjoint`	`DA` or `CA`	Type of adjoint: discrete adjoint or continuous adjoint
`lin_or_nonlin`	`nonlin` or `linear`	Iteration procedure: nonlinear using a Newton method or linear using the active iteration method
`param`	structure	The nondimensional parameters: γ, ζ, n, τ, X_w, L_w, X_h, L_h, R_u, R_d, ρ_u, ρ_d, $k_u s^{-1}$, $k_d s^{-1}$, c_u, and c_d
`scheme`	`.N .s0 .itmax`	The number of elements N, the starting value of s, and the number of iterations, J for the active iteration method
`TT_int`	cell array	The base state sensitivities to be tested, e.g., `{'t','h'}`, `{'all'}`, or {}
`TT_ext`	cell array	The external sensitivities to be tested, e.g., `{'X_w','R_u'}`, `{'all'}`, or {}

Output arguments (`fun_Helm.m`)

name	values/type	description/contents
`emode`	structure	For `DA`: discretization points $\mathbf{x}$; left eigenvector $\mathbf{p}^\dagger$; eigenvalue s; right eigenvector $\mathbf{p}$; discrete receptivities $\dot{m}^\dagger_{\overline{\rho}}$, $\mathbf{f}^\dagger_{\overline{\rho}}$, and $\dot{q}^\dagger_{\overline{p}}$; and mass matrix $\mathbf{M}$ For `CA`: discretization points $\mathbf{x}$, right eigenvector $\mathbf{p}^\dagger$, and continuous receptivities $\dot{m}^\dagger_{\overline{\rho}}$, $\mathbf{f}^\dagger_{\overline{\rho}}$, and $\dot{q}^\dagger_{\overline{p}}$
`ds_int`	structure	For `DA`: base state sensitivities $(\partial s/\partial n)$, $(\partial s/\partial k_u)$, and $(\partial s/\partial k_d)$; discrete base state sensitivities $(\partial s/\partial \tau)$, $(\partial s/\partial \mathbf{h})$, $(\partial s/\partial \mathbf{w}_{\overline{\rho}})$, and $(\partial s/\partial \overline{\mathbf{v}})$; discrete feedback sensitivities $(\partial s/\partial \dot{m}_{\overline{\rho},u})$, $(\partial s/\partial \dot{m}_{\overline{\rho},p})$, $(\partial s/\partial \mathbf{f}_{\overline{\rho},u})$, $(\partial s/\partial \mathbf{f}_{\overline{\rho},p})$, $(\partial s/\partial \dot{q}_{\overline{p},u})$, and $(\partial s/\partial \dot{q}_{\overline{p},p})$ For `CA`: base state sensitivities $(\partial s/\partial n)$, $(\partial s/\partial k_u)$, and $(\partial s/\partial k_d)$; continuous base state sensitivities $(\partial s/\partial \tau)_{\text{cont}}$, $(\partial s/\partial \mathbf{h})_{\text{cont}}$, $(\partial s/\partial \mathbf{w}_{\overline{\rho}})_{\text{cont}}$, and $(\partial s/\partial \overline{\mathbf{v}})_{\text{cont}}$; continuous feedback sensitivities $(\partial s/\partial \dot{m}_{\overline{\rho},u})_{\text{cont}}$, $(\partial s/\partial \dot{m}_{\overline{\rho},p})_{\text{cont}}$, $(\partial s/\partial \mathbf{f}_{\overline{\rho},u})_{\text{cont}}$, $(\partial s/\partial \mathbf{f}_{\overline{\rho},p})_{\text{cont}}$, $(\partial s/\partial \dot{q}_{\overline{p},u})_{\text{cont}}$, and $(\partial s/\partial \dot{q}_{\overline{p},p})_{\text{cont}}$
`ds_ext`	structure	$\partial s/\partial n$, $\partial s/\partial \tau$, $\partial s/\partial X_w$, $\partial s/\partial L_w$, $\partial s/\partial X_h$, $\partial s/\partial L_h$, $\partial s/\partial R_u$, $\partial s/\partial R_d$

`mat_FD.m`

Generate the Gauss-Lobatto grid points $\mathbf{x}$ and the differentiation matrix $\mathbf{D}$.
Generate the mass matrix $\mathbf{M}$ for the finite-difference schemes `FDS` and `FDW`.
Calculate the density at $\mathbf{x}$ with `fun_rh.m` and create the density matrix $\mathbf{V}$.
Calculate the heat release at $\mathbf{x}$ with `fun_h.m`.
Calculate the measurement profile and its derivative at $\mathbf{x}$ with `fun_wr.m`.
Generate the time delay vector τ at $\mathbf{x}$.

Input arguments

name	values/type	description/contents
`param`	structure	as for `fun_Helm.m`.
`N`	`N`	The number of elements N

Output arguments

name	values/type	description/contents
`pos`	`.x`	The vector $\mathbf{x}$
`mat`	structure	The matrices $\mathbf{D}$, $\mathbf{M}$, and $\mathbf{V}$ and the vectors τ, $\mathbf{h}$, $\mathbf{w}_{\overline{\rho}}$, and $\mathbf{w}'_{\overline{\rho}}$

`mat_FE.m`

Generate equispaced points for P0 and P1 functions $\mathbf{x}_0$ and $\mathbf{x}_1$.
Generate the differentiation matrix $\mathbf{D}_{01}$ and mass matrices $\mathbf{M}_{00}$, $\mathbf{M}_{01}$, and $\mathbf{M}_{11}$.
Calculate the density at $\mathbf{x}_0$ with `fun_rh.m` and create the density matrix $\mathbf{V}_{00}$.
Calculate the heat release at $\mathbf{x}_1$ with `fun_h.m`.
Calculate the measurement profile at $\mathbf{x}_0$ with `fun_wr.m`.
Calculate the derivative of the measurement profile at $\mathbf{x}_1$.
Generate the time delay vector τ at $\mathbf{x}_1$.

Input arguments

name	values/type	description/contents
`param`	structure	as for `fun_Helm.m`.
`N`	`N`	The number of elements N

Output arguments

name	values/type	description/contents
`pos`	`.x0`, `.x1`	The vectors $\mathbf{x}_0$ and $\mathbf{x}_1$
`mat`	structure	The matrices $\mathbf{D}_{01}$, $\mathbf{M}_{00}$, $\mathbf{M}_{01}$, $\mathbf{M}_{11}$, and $\mathbf{V}_{00}$ and the vectors $\mathbf{h}_1$, $\mathbf{w}_{\overline{\rho}0}$, and $\mathbf{w}'_{\overline{\rho}1}$

`mat_SBP.m`

Generate $N+1$ equispaced points $\mathbf{x}_1$ and their midpoints $\mathbf{x}_0$.
Generate the first-order differentiation matrix $\mathbf{D}_1$ and mass matrices $\mathbf{M}_{00}$, $\mathbf{M}_{01}$, and $\mathbf{M}$.
Generate the first derivative operator at the boundaries $\mathbf{S}$.
Generate a building block matrix for the second derivative operator: $\mathbf{D}_{01}$.
Generate building block matrices for the simultaneous approximation term: $\mathbf{E}_d$, $\mathbf{E}_u$, and $\mathbf{I}$.
Calculate the density at $\mathbf{x}_0$ and $\mathbf{x}_1$ with `fun_rh.m` and create the density matrices $\mathbf{V}_{00}$ and $\mathbf{V}_{11}$.
Calculate the heat release at $\mathbf{x}_1$ with `fun_h.m`.
Calculate the measurement profile at $\mathbf{x}_1$ with `fun_wr.m`.
Calculate the derivative of the measurement profile at $\mathbf{x}_1$.
Generate the time delay vector τ at $\mathbf{x}_1$.

Input arguments

name	values/type	description/contents
`param`	structure	as for `fun_Helm.m`.
`N`	`N`	The number of elements N

Output arguments

name	values/type	description/contents
`pos`	`.x0`, `.x1`	The vectors $\mathbf{x}_0$ and $\mathbf{x}_1$
`mat`	structure	The matrices $\mathbf{D}_1$, $\mathbf{D}_{01}$, $\mathbf{M}$, $\mathbf{M}_{00}$, $\mathbf{M}_{01}$, $\mathbf{V}_{00}$, $\mathbf{V}_{11}$, $\mathbf{S}$, $\mathbf{E}_d$, $\mathbf{E}_u$, and $\mathbf{I}$ and the vectors $\mathbf{h}$, $\mathbf{w}_{\overline{\rho}}$, and $\mathbf{w}'_{\overline{\rho}}$

`mat_AC_**_DA.m`

Construct the **A**, **C**, and $d\mathbf{A}/ds$ matrices for the direct equations in `FDS` (13), `FEW` (15), `FDW` (16), and `SBP` (17).
Apply boundary conditions with `fun_bcs_strong.m` or `fun_bcs_weak.m`.
Generate the matrices that map from **p** to **u** and from $\mathbf{p}^\dagger$ to the receptivities $\dot{m}^\dagger_{\overline{\rho}}$, $\mathbf{F}^\dagger_{\overline{\rho},}$, and $\dot{q}^\dagger_{\overline{p}}$.
Generate $(d\mathbf{A}/db)_l$ and $(d\mathbf{A}/db)_r$ for all the internal parameters b.
(These are the terms in Table II before they have been multiplied by $\mathbf{p}^\dagger$ and **p**.)
Apply boundary conditions to $(d\mathbf{A}/db)_l$ and $(d\mathbf{A}/db)_r$.

Input arguments

name	values/type	description/contents
`mat`	structure	as for `mat_FD.m`, `mat_FE.m`, or `mat_SBP.m`
`param`	structure	as for `fun_Helm.m`.
`N`	`N`	The number of elements N
`s`	`s`	The eigenvalue s

Output arguments

name	values/type	description/contents
`A`	matrix	The matrix **A** with boundary conditions applied
`C`	matrix	The matrix **C** with boundary conditions applied
`dAds`	matrix	The matrix $d\mathbf{A}/ds$ with boundary conditions applied
`T`	structure	Matrices that convert **p** and $\mathbf{p}^\dagger$ into **u** and the receptivities
`dA`	structure	Matrices and vectors $(d\mathbf{A}/db)_l$ and $(d\mathbf{A}/db)_r$
`ds_int`	structure	The structure in `fun_Helm.m` with all values set to zero

`mat_AC_**_CA.m`

Construct **A**, **C**, and $d\mathbf{A}/ds$ matrices for the continuous adjoint in `FDS` (27), `FEW` (28), `FDW` (29), and `SBP` (30).
Apply boundary conditions with `fun_bcs_strong.m` or `fun_bcs_weak.m`.
Generate the matrices that convert from $\mathbf{p}^\dagger$ to the receptivities $\dot{m}^\dagger_{\overline{\rho}}$, $\mathbf{F}^\dagger_{\overline{\rho},}$, and $\dot{q}^\dagger_{\overline{p}}$.

Input arguments

name	values/type	description/contents
`mat`	structure	as for `mat_FD.m`, `mat_FE.m`, or `mat_SBP.m`
`param`	structure	as for `fun_Helm.m`.
`N`	`N`	The number of elements N
`conjs`	`conjs`	The complex conjugate of the eigenvalue s

Output arguments

name	values/type	description/contents
`A`	matrix	The matrix **A** with boundary conditions applied
`C`	matrix	The matrix **C** with boundary conditions applied
`dAds`	matrix	The matrix $d\mathbf{A}/ds$ with boundary conditions applied
`T`	structure	Matrices that convert $\mathbf{p}^\dagger$ into the receptivities

Remaining functions

name	description
`fun_bcs_strong.m`	Apply the boundary conditions to the strong form equations.
`fun_bcs_weak.m`	Apply the boundary conditions to the weak form equations.
`fun_ds_CA.m`	Evaluate the internal sensitivities in the continuous adjoint framework.
`fun_ds_DA.m`	Evaluate the internal sensitivities in the discrete adjoint framework.
`fun_eig_nearest.m`	Solve $\mathbf{Ap} = s^2\mathbf{Cp}$ and select the eigenmode with s closest to s_0.
`fun_ext_int_CA.m`	Evaluate the external sensitivities in the continuous adjoint framework.
`fun_ext_int_DA.m`	Evaluate the external sensitivities in the discrete adjoint framework.
`fun_h.m`	Set the heat release envelope $\mathbf{h}$ and its partial derivatives.
`fun_kukd.m`	Calculate the Robin boundary coefficients k_u and k_d.
`fun_nondim.m`	Convert the dimensional parameters to nondimensional parameters.
`fun_normalize.m`	Normalize $\mathbf{p}$ such that $\mathbf{p}^T\mathbf{Mp} = 1$.
`fun_param_dim.m`	Set the dimensional parameters.
`fun_rh.m`	Set the density profile and its partial derivatives.
`fun_set_s0.m`	Use a traveling wave method to estimate s_0 for the requested mode.
`fun_TT.m`	Perform a Taylor test on the fields held in `TT_int` and `TT_ext`.
`fun_wr.m`	Set the measurement envelope $\mathbf{w}$ and its partial derivatives.
`unwrap_*.m`	Unwrap variables from structure $*$.
`wrap_*.m`	Wrap variables into structure $*$.

[1] T. C. Lieuwen and V. Yang, *Combustion Instabilities in Gas Turbine Engines: Operational Experience, Fundamental Mechanisms, and Modeling* (AIAA, Reston, 2005).

[2] J. W. S. B. Rayleigh, The explanation of certain acoustical phenomena, Nature (London) **18**, 319 (1878).

[3] B.-T. Chu, On the energy transfer to small disturbances in fluid flow (Part I), Acta Mech. **1**, 215 (1965).

[4] M. P. Juniper and R. I. Sujith, Sensitivity and nonlinearity of thermoacoustic oscillations, Annu. Rev. Fluid Mech. **50**, 661 (2018).

[5] T. C. Lieuwen and K. R. McManus, Combustion dynamics in lean-premixed prevaporized (LPP) gas turbines, J. Propul. Power **19**, 721 (2003).

[6] H. C. Mongia, T. J. Held, G. C. Hsiao, and R. P. Pandalai, Challenges and progress in controlling dynamics in gas turbine combustors introduction, J. Propul. Power **19**, 822 (2003).

[7] Y. Huang and V. Yang, Dynamics and stability of lean-premixed swirl-stabilized combustion, Prog. Energy Combust. Sci. **35**, 293 (2009).

[8] G. Richards, D. L. Strauss, and E. H. Robey, Passive control of combustion dynamics in stationary gas turbines, J. Propul. Power **19**, 795 (2003).

[9] L. Crocco and S.-I. Cheng, *Theory of Combustion Instability in Liquid Propellant Rocket Motors* (Butterworths, London, 1956).

[10] P. Luchini and A. Bottaro, Adjoint equations in stability analysis, Annu. Rev. Fluid Mech. **46**, 493 (2014).

[11] L. Magri and M. P. Juniper, Sensitivity analysis of a time-delayed thermo-acoustic system via an adjoint-based approach, J. Fluid Mech. **719**, 183 (2013).

[12] L. Magri and M. P. Juniper, Global modes, receptivity, and sensitivity analysis of diffusion flames coupled with duct acoustics, J. Fluid Mech. **752**, 237 (2014).

[13] T. Sayadi, V. Le Chenadec, P. J. Schmid, F. Richecoeur, and M. Massot, Thermoacoustic instability—A dynamical system and time domain analysis, J. Fluid Mech. **753**, 448 (2014).

[14] J. G. Aguilar, L. Magri, and M. P. Juniper, Adjoint-based sensitivity analysis of low-order thermoacoustic networks using a wave-based approach, J. Comput. Phys. **341**, 163 (2017).

[15] J. G. Aguilar and M. P. Juniper, *Proceedings of GPPS Forum 18, Zurich, 2018* (GPPS, Zug, 2018), paper GPPS-2018-0024.
[16] J. G. Aguilar and M. P. Juniper, *ASME Turbo Expo: Turbomachinery Technical Conference and Exposition, Oslo, 2018* (ASME, New York, 2018), paper GT2018-75692.
[17] S. R. Stow and A. P. Dowling, *ASME Turbo Expo 2001: Power for Land, Sea, and Air, New Orleans, 2001* (ASME, New York, 2001), paper 2001-GT-0037.
[18] S. R. Stow and A. P. Dowling, *ASME Turbo Expo 2004: Power for Land, Sea, and Air, Vienna, 2004* (ASME, New York, 2004), paper GT2004-54245.
[19] M. P. Juniper, L. Magri, M. Bauerheim, and F. Nicoud, *Centre for Turbulence Research, Proceedings of the Summer Program 2014* (Stanford University, Stanford, 2014).
[20] G. A. Mensah and J. P. Moeck, Acoustic damper placement and tuning for annular combustors: An adjoint-based optimization study, J. Eng. Gas Turbines Power **139**, 061501 (2017).
[21] G. A. Mensah, L. Magri, and J. P. Moeck, Methods for the calculation of thermoacoustic stability boundaries and Monte Carlo-free uncertainty quantification, J. Eng. Gas Turbines Power **140**, 061501 (2018).
[22] C. F. Silva, L. Magri, T. Runte, and W. Polifke, Uncertainty quantification of growth rates of thermoacoustic instability by an adjoint helmholtz solver, J. Eng. Gas Turbines Power **139**, 011901 (2018).
[23] G. A. Mensah, L. Magri, A. Orchini, and J. P. Moeck, *ASME Turbo Expo: Turbomachinery Technical Conference and Exposition, Oslo, 2018* (ASME, New York, 2018), paper GT2018-76797.
[24] A. Ndiaye, Quantification des incertitudes pour la prédiction des instabilités thermo-acoustiques dans les chambres de combustion, Ph.D. thesis, Université de Montpellier, 2017, Chap. 7.
[25] F. Nicoud, L. Benoit, C. Sensiau, and T. Poinsot, Acoustic modes in combustors with complex impedances and multidimensional active flames, AIAA J. **45**, 426 (2007).
[26] L. N. Trefethen, *Spectral Methods in Matlab* (SIAM, Philadelphia, 2000).
[27] R. Kamakoti and C. Pantano, High-order narrow stencil finite-difference approximations of second-order derivatives involving variable coefficients, SIAM J. Sci. Comput. **31**, 4222 (2009).
[28] J. E. Hicken and D. W. Zingg, Superconvergent functional estimates form summation-by-parts finite-difference discretizations, SIAM J. Sci. Comput. **33**, 893 (2011).
[29] J. Berg and J. Nordström, Duality based boundary conditions and dual consistent finite difference discretizations of the Navier-Stokes and Euler equations, J. Comput. Phys. **259**, 135 (2014).
[30] S. Eriksson, A dual consistent finite difference method with narrow stencil second derivative operators, J. Sci. Comput. **75**, 906 (2018).
[31] K. Mattsson and J. Nordström, Summation by parts operators for finite difference approximations of second derivatives, J. Comput. Phys. **199**, 503 (2004).
[32] T. Nystrand, Summation by part methods for Poisson's equation with discontinuous variable coefficients, Ph.D. thesis, Uppsala Universitet, 2014.
[33] G. Rigas, N. P. Jamieson, L. K. B. Li, and M. P. Juniper, Experimental sensitivity analysis and control of thermoacoustic systems, J. Fluid Mech. **787**, R1 (2016).
[34] See Supplemental Material at http://link.aps.org/supplemental/10.1103/PhysRevFluids.3.110509 for MATLAB files.
[35] G. J. Chandler, M. P. Juniper, J. W. Nichols, and P. J. Schmid, Adjoint algorithms for the Navier-Stokes equations in the low Mach number limit, J. Comput. Phys. **231**, 1900 (2012).
[36] L. Magri, M. Bauerheim, and M. P. Juniper, Stability analysis of thermo-acoustic nonlinear eigenproblems in annular combustors. Part I. Sensitivity, J. Comput. Phys. **325**, 395 (2016).
[37] J.-M. Chomaz, Global instabilities in spatially developing flows: Non-normality and nonlinearity, Annu. Rev. Fluid Mech. **37**, 357 (2005).
[38] D. Sipp, O. Marquet, P. Meliga, and A. Barbagallo, Dynamics and control of global instabilities in open-flows: A linearized approach, Appl. Mech. Rev. **63**, 030801 (2010).
[39] M. P. Juniper and L. Magri, *Progress in Flow Instability Analysis and Laminar-Turbulent Transition Modeling* (von Karman Institute for Fluid Dynamics, Sint-Genesius-Rode, 2014).

[40] L. Magri, M. Bauerheim, F. Nicoud, and M. P. Juniper, Stability analysis of thermo-acoustic nonlinear eigenproblems in annular combustors. Part II. Uncertainty quantification, J. Comput. Phys. **325**, 411 (2016).
[41] D. S. Miller, *Internal Flow Systems* (BHRA Fluid Engineering, Cranfield, 1978).
[42] N. P. Jamieson and M. P. Juniper, Experimental sensitivity analysis of a linearly stable thermoacoustic system via a pulsed forcing technique, Exp. Fluids **58**, 123 (2017).
[43] J. Aguilar, Sensitivity analysis and optimization in low order thermoacoustic models, Ph.D. thesis, University of Cambridge, 2018.
[44] S. W. Rienstra and A. Hirschberg, *An Introduction to Acoustics* (Eindhoven University of Technology, Eindhoven, 2006).
[45] D. Funaro and D. Gottlieb, A new method of imposing boundary conditions in pseudospectral approximations of hyperbolic equations, Math. Comput. **51**, 599 (1988).
[46] D. C. Del Rey Fernández, J. E. Hicken, and D. W. Zingg, Review of summation-by-parts operators with simultaneous approximation terms for the numerical solution of partial differential equations, Comput. Fluids **95**, 171 (2014).